UCLA CAM Report 07-49, November 2007

Asymmetric and Symmetric Unbiased Image Registration: Statistical Assessment of Performance

UCLA CAM Report 07-49, 2007

Igor Yanovsky · Paul Thompson · Stanley Osher · Alex Leow

November, 2007

Abstract In this paper, we propose to investigate the asymmetric version of the Unbiased registration and, for the first time, analyze unbiased models with mutual information based matching functionals. Most importantly, this paper examines the reproducibility and the power to detect real changes of different computational techniques in TBM. In particular, we compare matching functionals (sum of squared differences and mutual information), as well as large deformation registration schemes (symmetric and asymmetric unbiased registration and viscous fluid registration) using serial MRI scans of ten normal elderly patients from the preparatory phase of the Alzheimer's Disease Neuroimaging Initiative (ADNI) and ten Alzheimer's subjects from the ADNI follow-up phase. Our results show that the unbiased methods, both symmetric and asymmetric, have higher reproducibility. The unbiased methods are less likely to produce changes in the absence of any real physiological change. Moreover, they are also better in detecting biological deformations by penalizing any bias in the corresponding statistical maps.

Keywords Mutual information · image registration · computational anatomy

This work was supported in part by NIH Grants U54 RR021813 and U01 AG024904. Igor Yanovsky was also supported by NSF VIGRE Grant DMS-0601395 and CCB-NIH Grant 30886. Paul Thompson was also supported by Grants R21 RR019771, EB01651, AG016570, NS049194, and P41 RR13642.

I. Yanovsky
University of California, Los Angeles
Department of Mathematics
Los Angeles, CA 90095
E-mail: yanovsky@math.ucla.edu

P. Thompson
UCLA School of Medicine
Laboratory of Neuro Imaging
Los Angeles, CA 90095
E-mail: thompson@loni.ucla.edu

S. Osher
University of California, Los Angeles
Department of Mathematics
Los Angeles, CA 90095
E-mail: sjo@math.ucla.edu

A. Leow
UCLA School of Medicine
Laboratory of Neuro Imaging
Los Angeles, CA 90095
E-mail: feuillet@ucla.edu

1 Introduction

In recent years, computational neuroimaging has become an exciting interdisciplinary field with many applications in functional and anatomic brain mapping, image-guided surgery, and multimodality image fusion [1–9]. The goal of image registration is to align, or spatially normalize, one image to another. In multi-subject studies, this reduces subject-specific anatomic differences by deforming individual images onto a population average brain template. When applied to serial scans of human brain, image registration offers tremendous power in detecting the earliest signs of illness, understanding normal brain development or aging, and monitoring disease progression [10–13]. Recently, there has been an expanding literature on various nonrigid registration techniques, with different image matching functionals, regularization schemes, and numerical implementations. In [14, 15] our group systematically examined the statistical properties of Jacobian maps (the determinant of the local Jacobian operator applied to the deformations), and proposed an *unbiased* large - deformation image registration approach. In this context, unbiased means that the Jacobian determinants

of the deformations recovered between a pair of images follow a log-normal distribution, with zero mean after log-transformation. We argued that this distribution is beneficial when recovering change in regions of homogeneous intensity, and in ensuring symmetrical results when the order of two images being registered is switched. We applied this method to a longitudinal MRI dataset from a single subject, and showed promising results in eliminating spurious signals. We also noticed that different registration techniques, when applied to the same longitudinal dataset, may sometimes yield visually very different Jacobian maps, causing problems in interpreting local structural changes. Given this ambiguity and the increasing use of registration methods to measure brain change, more information is required concerning the baseline stability, reproducibility, and statistical properties of signals generated by different nonrigid registration techniques.

In this paper, we introduce a novel Asymmetric Unbiased model (by contrast with the Symmetric Unbiased model) and, for the first time, we analyze unbiased models with mutual information based matching functionals (prior work has focused on the case where the summed squared intensity difference is used as the criterion for registration). Most importantly, we aim to provide quality calibrations for different non-rigid registration techniques in TBM. In particular, we compare two common matching functionals: L^2, or the sum of squared intensity differences, versus mutual information, and three regularization techniques (fluid registration versus the Asymmetric Unbiased and Symmetric Unbiased techniques). Our experiments are designed to decide which registration method is more reproducible, more reliable, and offers less artifactual variability in regions of homogeneous image intensity. Following our analyses in the preparatory phase of the Alzheimer's Disease Neuroimaging Initiative (ADNI) [16], the foundation of our calibrations is based on the assumption that, by scanning healthy normal human subjects twice over a 2-week period using the same protocol, serial MRI scan pairs should not show any systematic biological change. Therefore, any regional structural differences detected using TBM over such a short interval may be assumed to be errors. We apply statistical analysis to the profile of these errors, providing information on the reliability, reproducibility and variability of different registration techniques. Moreover, serial images of 10 subjects from the ADNI follow-up phase (images acquired one year apart) were analyzed in a similar fashion and compared to the ADNI baseline data. In images collected one year apart, real anatomical changes are present; neurobiological changes due to aging and dementia include widespread cell shrinkage, regional gray and white matter atrophy and expansion of fluid-filled spaces in the brain. Thus, a good computational technique should be able to differentiate between longitudinal image pairs collected for the ADNI baseline (2-week) and follow-up (1-year) phases. We refer to prior papers for details of the ADNI acquisition protocol, but briefly, all subjects were scanned with a standardized MRI protocol, developed after a major effort evaluating and comparing 3D T1-weighted sequences for morphometric analyses [17].

In the experiments that follow, all scans were collected according to the standard ADNI MRI protocol (http://www.loni.ucla.edu/ADNI/Research/Cores/), which acquires a high-resolution sagittal T1-weighted 3D MP-RAGE sequence for each subject, with a reconstructed voxel size of $0.9375 \times 0.9375 \times 1.2\, mm^3$. Additional image corrections were also applied, using a processing pipeline at the Mayo Clinic, consisting of: (1) a procedure termed *GradWarp* for correction of geometric distortion due to gradient non-linearity [18], (2) a "B1-correction", to adjust for image intensity non-uniformity using B1 calibration scans [17], (3) "N3" bias field correction, for reducing intensity inhomogeneity [19], and (4) geometrical scaling, according to a phantom scan acquired for each subject [17], to adjust for scanner- and session-specific calibration errors. Additional phantom-based geometric corrections were applied to ensure spatial calibration was kept within a specific tolerance level for each scanner involved in the ADNI study [20].

At this point, we would like to motivate the unbiased approach, which couples the computation of deformations with statistical analyses on the resulting Jacobian maps. As a result, the unbiased approach ensures that deformations have intuitive axiomatic properties by penalizing any bias in the corresponding statistical maps. In the following sections, we describe the mathematical foundations of this approach, define energy functionals for minimization, and perform thorough statistical analyses to demonstrate the advantages of the unbiased registration models.

2 Unbiased Large-Deformation Image Registration

We first introduce the notation used in this paper. Throughout this paper, we denote the vectors by bold fonts and scalars by regular fonts. Let Ω be an open and bounded domain in $\mathbb{R}^n$, for arbitrary n. Without loss of generality, assume that the volume of Ω is 1, i.e. $|\Omega| = 1$. Let $I_1 : \Omega \to \mathbb{R}$ and $I_2 : \Omega \to \mathbb{R}$ be the two images to be registered. We seek to estimate a transformation $\mathbf{g} : \Omega \to \Omega$ such that I_2 matches I_1 when deformed

by $\mathbf{g}$. In this paper, we will restrict this mapping to be differentiable, one-to-one, and onto. We denote the Jacobian matrix of a deformation $\mathbf{g}$ to be $D\mathbf{g}$. The inverse mapping of $\mathbf{g}$ is denoted by $\mathbf{g}^{-1}$.

The displacement field $\mathbf{u}(\mathbf{x})$ from the position $\mathbf{x}$ in the deformed image $I_2 \circ \mathbf{g}(\mathbf{x})$ back to $I_2(\mathbf{x})$ is defined in terms of the deformation $\mathbf{g}(\mathbf{x})$ by the expression $\mathbf{g}(\mathbf{x}) = \mathbf{x} - \mathbf{u}(\mathbf{x})$ at every point $\mathbf{x} \in \Omega$. Thus, we consider the problems of finding $\mathbf{g}$ and $\mathbf{u}$ to be equivalent. It is sometimes more convenient to write expressions in terms of either $\mathbf{g}$ or $\mathbf{u}$. For instance, we can denote the determinant of the Jacobian matrix of deformation $\mathbf{g}$ as either $|D\mathbf{g}(\mathbf{x})|$ or $|D(\mathbf{x} - \mathbf{u}(\mathbf{x}))|$.

We now describe the construction of the Unbiased Large-Deformation Image Registration. We associate three probability density functions (PDFs) to $\mathbf{g}$, $\mathbf{g}^{-1}$, and the identity mapping $\mathbf{id}$:

$$P_{\mathbf{g}}(\mathbf{x}) = |D\mathbf{g}(\mathbf{x})|, \tag{1}$$

$$P_{\mathbf{g}^{-1}}(\mathbf{x}) = |D\mathbf{g}^{-1}(\mathbf{x})|, \tag{2}$$

$$P_{\mathbf{id}}(\mathbf{x}) = 1. \tag{3}$$

By associating deformations with their corresponding global density maps, we can now apply information theory to quantify the magnitude of deformations. In our approach, we choose the Kullback-Leibler (KL) divergence and symmetric Kullback-Leibler (SKL) distance. The KL divergence between two probability density functions, X and Y, is defined as

$$KL(X,Y) = \int_{\Omega} X \log \frac{X}{Y} d\mathbf{x} \geq 0. \tag{4}$$

We define the SKL distance as

$$SKL(X,Y) = KL(X,Y) + KL(Y,X). \tag{5}$$

The Unbiased method solves for the deformation $\mathbf{g}$ (or, equivalently, for the displacement $\mathbf{u}$) minimizing the energy functional E, consisting of the image matching term F and the regularizing term R which is based on KL divergence or SKL distance. The fidelity term F dependents on I_2 and I_1, as well as the displacement $\mathbf{u}$. The general minimization problem can be written as

$$\begin{aligned} &E(I_1, I_2, \mathbf{u}) = F(I_1, I_2, \mathbf{u}) + \lambda R(\mathbf{u}), \\ &\qquad \inf_{\mathbf{u}} E(I_1, I_2, \mathbf{u}). \end{aligned} \tag{6}$$

Here, $\lambda > 0$ is a weighting parameter.

2.1 Asymmetric Unbiased Registration

To quantify the magnitude of deformation $\mathbf{g}$, in this paper we introduce a new regularization term R_{KL}, which is an asymmetric measure between $P_{\mathbf{id}}$ and $P_{\mathbf{g}}$:

$$R_{KL}(\mathbf{g}) = KL(P_{\mathbf{id}}, P_{\mathbf{g}}). \tag{7}$$

This regularization term can be shown to be

$$\begin{aligned} R_{KL}(\mathbf{g}) &= \int_{\Omega} P_{\mathbf{id}} \log \frac{P_{\mathbf{id}}}{P_{\mathbf{g}}} \, d\mathbf{x} = \int_{\Omega} -\log |D\mathbf{g}(\mathbf{x})| d\mathbf{x} \\ &= \int_{\Omega} |D\mathbf{g}^{-1}(\mathbf{y})| \log |D\mathbf{g}^{-1}(\mathbf{y})| d\mathbf{y}. \end{aligned} \tag{8}$$

Thus, the energy functional in (6) implementing Asymmetric Unbiased registration can be written as

$$\begin{aligned} E(I_1, I_2, \mathbf{u}) &= F(I_1, I_2, \mathbf{u}) \\ &\quad -\lambda \int_{\Omega} \log |D(\mathbf{x} - \mathbf{u}(\mathbf{x}))| d\mathbf{x}, \end{aligned} \tag{9}$$

for some distance measure F between $I_2(\mathbf{x} - \mathbf{u})$ and $I_1(\mathbf{x})$.

2.2 Symmetric Unbiased Registration

In this section, we describe the regularization functional based on the symmetric KL distance between $P_{\mathbf{id}}$ and $P_{\mathbf{g}}$:

$$R_{SKL}(\mathbf{g}) = SKL(P_{\mathbf{id}}, P_{\mathbf{g}}). \tag{10}$$

As shown in [14,15] the regularization term is linked to statistics on Jacobian maps as follows

$$\begin{aligned} R_{SKL}(\mathbf{g}) &= KL(P_{\mathbf{g}}, P_{\mathbf{id}}) + KL(P_{\mathbf{g}^{-1}}, P_{\mathbf{id}}) \\ &= KL(P_{\mathbf{g}}, P_{\mathbf{id}}) + KL(P_{\mathbf{id}}, P_{\mathbf{g}}) \\ &= KL(P_{\mathbf{id}}, P_{\mathbf{g}^{-1}}) + KL(P_{\mathbf{id}}, P_{\mathbf{g}}) \\ &= KL(P_{\mathbf{id}}, P_{\mathbf{g}^{-1}}) + KL(P_{\mathbf{g}^{-1}}, P_{\mathbf{id}}) \\ &= \int_{\Omega} \big(|D\mathbf{g}(\mathbf{x})| - 1\big) \log |D\mathbf{g}(\mathbf{x})| d\mathbf{x} \\ &= \int_{\Omega} \big(|D\mathbf{g}^{-1}(\mathbf{y})| - 1\big) \log |D\mathbf{g}^{-1}(\mathbf{y})| d\mathbf{y}. \end{aligned} \tag{11}$$

The energy functional employing Symmetric Unbiased registration can be rewritten as

$$\begin{aligned} &E(I_1, I_2, \mathbf{u}) = F(I_1, I_2, \mathbf{u}) \\ &+\lambda \int_{\Omega} \big(|D(\mathbf{x} - \mathbf{u}(\mathbf{x}))| - 1\big) \log |D(\mathbf{x} - \mathbf{u}(\mathbf{x}))| d\mathbf{x}, \end{aligned} \tag{12}$$

for some distance measure F. Notice that the symmetric unbiased regularizing functional is pointwise nonnegative, while the asymmetric unbiased regularizer in (8) can take either positive or negative values locally.

3 Fidelity Metrics

In this paper, the matching functional F takes two forms: the L^2 norm (the sum of squared intensity differences) and MI (mutual information). These functionals have each been widely used in the past for nonrigid registration, to measure the intensity agreement between a deforming image and the target image. We briefly describe both distances in this section.

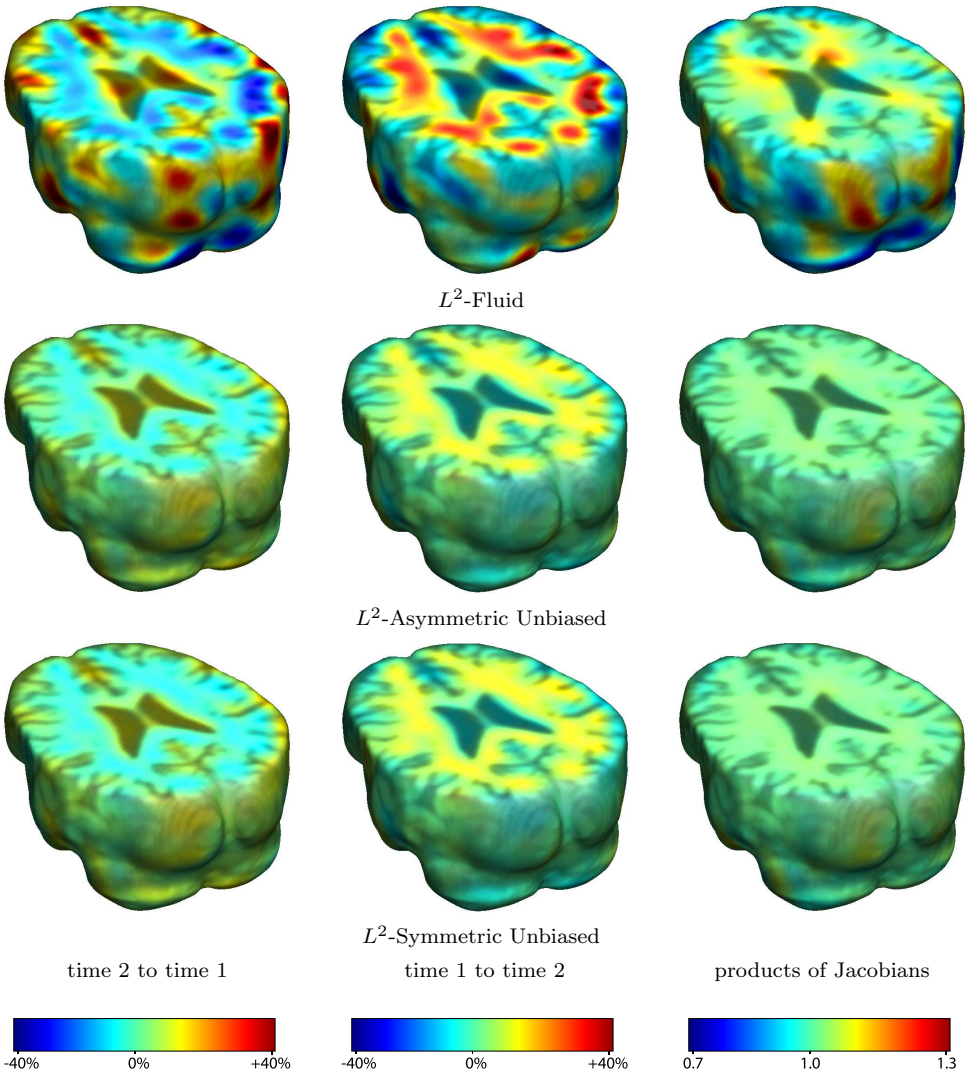

Fig. 1 Nonrigid registration was performed on an image pair from one of the subjects from the ADNI Baseline study (serial MRI images acquired two weeks apart) using L^2-Fluid (row 1), L^2-Asymmetric Unbiased (row 2), and L^2-Symmetric Unbiased (row 3) registration methods. Jacobian maps of deformations from time 2 to time 1 (column 1) and time 1 to time 2 (column 2) are superimposed on the target volumes. The unbiased methods generate less noisy Jacobian maps with values closer to 1; this shows the greater stability of the approach when no volumetric change is present. Column 3 examines the inverse consistency of deformation models. Products of Jacobian maps generated using all three models are shown, for forward direction (time 1 to time 2) and backward direction (time 2 to time 1). For the L^2-based unbiased methods, the products of the Jacobian maps are less noisy, with values closer to 1, showing better inverse consistency.

3.1 L^2-norm

The L^2-norm matching functional is suitable when the images have been acquired through similar sensors and thus are expected to present the same intensity range and distribution. The L^2 distance between the deformed image $I_2(\mathbf{x}-\mathbf{u})$ and target image $I_1(\mathbf{x})$ is defined as

$$F_{L^2}(I_1, I_2, \mathbf{u}) = \frac{1}{2}\int_{\Omega} \left(I_2(\mathbf{x}-\mathbf{u}(\mathbf{x})) - I_1(\mathbf{x})\right)^2 d\mathbf{x}. \quad (13)$$

Computing the first variation of functional F_{L^2} gives the following gradient

$$\partial_{\mathbf{u}} F_{L^2}(I_1, I_2, \mathbf{u}) = -[I_2(\mathbf{x}-\mathbf{u}(\mathbf{x})) - I_1(\mathbf{x})]\, \nabla I_2|_{\mathbf{x}-\mathbf{u}}. \quad (14)$$

3.2 Mutual Information

Mutual information is a measure of how much information one random variable has about another. The use of mutual information for image registration was first

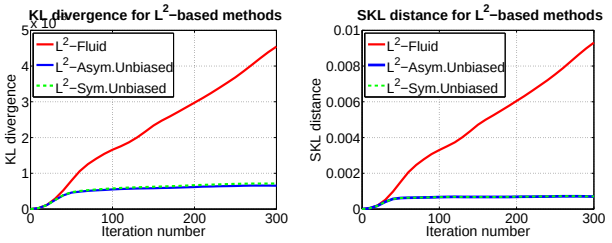

(a) KL divergence (b) SKL distance

Fig. 2 (a) KL divergence and (b) SKL distance per iteration are shown for L^2-Fluid (solid red), L^2-Asymmetric Unbiased (solid blue), and L^2-Symmetric Unbiased (dashed green) methods. For L^2-Fluid, both KL and SKL measures increase. Even though the Asymmetric Unbiased method explicitly minimizes the KL distance, and the Symmetric Unbiased model minimizes the SKL distance, both of the KL and SKL measures stabilize for both unbiased methods.

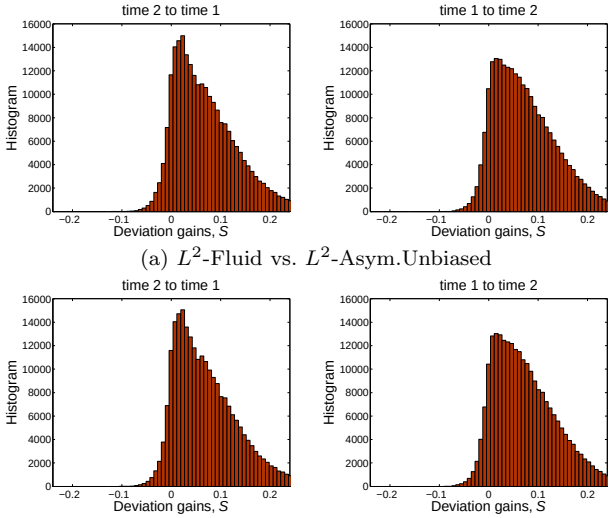

(a) L^2-Fluid vs. L^2-Asym.Unbiased

(b) L^2-Fluid vs. L^2-Sym.Unbiased

Fig. 3 Histograms of voxel-wise deviation gains (a) L^2-Fluid over L^2-Asymmetric Unbiased and (b) L^2-Fluid over L^2-Symmetric Unbiased for one of the subjects for the forward direction (time 2 to time 1) and backward direction (time 1 to time 2). The histograms are skewed to the right, indicating the superiority of Asymmetric Unbiased and Symmetric Unbiased registration methods over Fluid registration. A paired t test shows significance ($p < 0.0001$).

introduced in [21] and [22]. One of the main advantages of using mutual information is that it can be used to align images of different modalities, without requiring knowledge of the relationship (joint intensity distribution) of the two registered images. We refer the readers to [23–25] for relevant discussions on mutual information.

To define the mutual information between the deformed image $I_2(\mathbf{x}-\mathbf{u})$ and the target image $I_1(\mathbf{x})$, we follow the notations in [23], where p^{I_1} and $p_{\mathbf{u}}^{I_2}$ are used to denote the intensity distributions estimated from $I_1(\mathbf{x})$ and $I_2(\mathbf{x}-\mathbf{u})$, respectively. An estimate of their joint intensity distribution is denoted as $p_{\mathbf{u}}^{I_1,I_2}$. In this probabilistic framework, the link between two modalities is fully characterized by a joint density.

We let $i_1 = I_1(\mathbf{x})$, $i_2 = I_2(\mathbf{x}-\mathbf{u}(\mathbf{x}))$ denote intensity values at point $\mathbf{x} \in \Omega$. Given the displacement field $\mathbf{u}$, the mutual information computed from I_1 and I_2 is provided by

$$MI_{\mathbf{u}}^{I_1,I_2} = \int_{\mathbb{R}^2} p_{\mathbf{u}}^{I_1,I_2}(i_1,i_2)\, \log \frac{p_{\mathbf{u}}^{I_1,I_2}(i_1,i_2)}{p^{I_1}(i_1)p_{\mathbf{u}}^{I_2}(i_2)}\, di_1 di_2. \tag{15}$$

We seek to maximize the mutual information between $I_2(\mathbf{x}-\mathbf{u})$ and $I_1(\mathbf{x})$, or equivalently, minimize the negative of $MI_{\mathbf{u}}^{I_1,I_2}$:

$$F_{MI}(I_1,I_2,\mathbf{u}) = -MI_{\mathbf{u}}^{I_1,I_2}. \tag{16}$$

The gradient of (16) is derived in Appendix C and is given by

$$\partial_{\mathbf{u}} F_{MI}(\mathbf{u}) = \frac{1}{|\Omega|}\left[Q_{\mathbf{u}} * \frac{\partial \psi}{\partial \xi_2}\right](I_1(\mathbf{x}), I_2(\mathbf{x}-\mathbf{u}))\nabla I_2(\mathbf{x}-\mathbf{u}), \tag{17}$$

where $|\Omega|$ is the volume of Ω, $Q_{\mathbf{u}}$ is defined as

$$Q_{\mathbf{u}}(i_1,i_2) = 1 + \log \frac{p_{\mathbf{u}}^{I_1,I_2}(i_1,i_2)}{p^{I_1}(i_1)p_{\mathbf{u}}^{I_2}(i_2)}, \tag{18}$$

and $\psi(\xi_1,\xi_2)$ is a two-dimensional Parzen windowing kernel, which is used to estimate the joint intensity distribution from $I_2(\mathbf{x}-\mathbf{u})$ and $I_1(\mathbf{x})$. Here, we use the Gaussian kernel with variance σ^2:

$$\psi(\xi_1,\xi_2) = G_\sigma(\xi_1,\xi_2) = \frac{1}{2\pi\sigma^2} e^{\frac{-(\xi_1^2+\xi_2^2)}{2\sigma^2}}. \tag{19}$$

4 Minimization of Energy Functionals

In general, we expect minimizers of the energy functional $E(\mathbf{u})$ to exist. Computing the first variation of the functional in (6), we obtain the gradient of $E(I_1,I_2,\mathbf{u})$, namely $\partial_{\mathbf{u}} E(I_1,I_2,\mathbf{u})$. We define the force field $\mathbf{f}$, which drives I_2 into registration with I_1, as

$$\begin{aligned}\mathbf{f}(\mathbf{x},\mathbf{u}) &= \partial_{\mathbf{u}} E(I_1,I_2,\mathbf{u}) \\ &= \partial_{\mathbf{u}} F(I_1,I_2,\mathbf{u}) + \lambda \partial_{\mathbf{u}} R(\mathbf{u}).\end{aligned} \tag{20}$$

Here, $R(\mathbf{u})$ is either $R_{KL}(\mathbf{u})$ or $R_{SKL}(\mathbf{u})$. Explicit expressions for components of $\partial_{\mathbf{u}} R(\mathbf{u})$, in both cases, are derived in Appendices A and B for two and three dimensional cases, respectively. Also, the gradient $\partial_{\mathbf{u}} F(I_1,I_2,\mathbf{u})$ depends on the choice of the fidelity term.

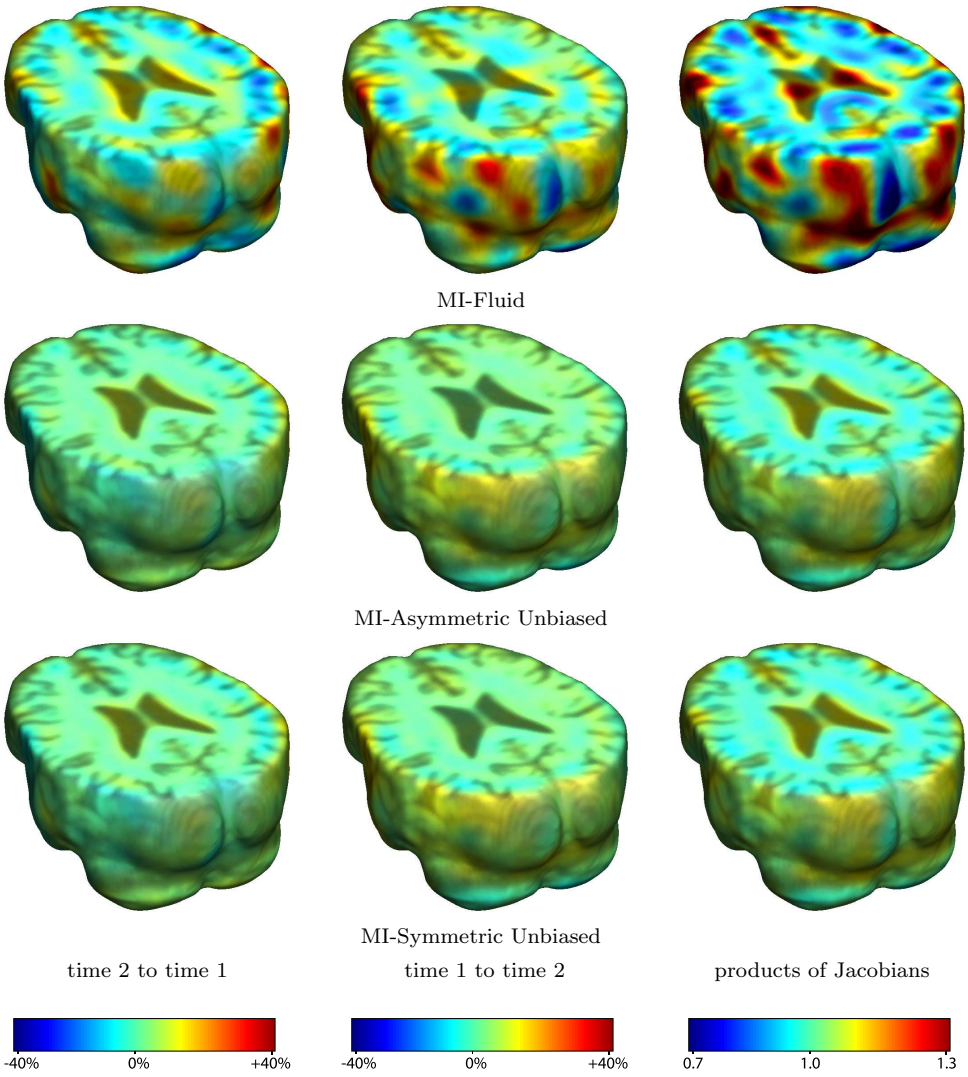

Fig. 4 Nonrigid registration was performed on an image pair from one of the subjects from the ADNI Baseline study (serial MRI images acquired two weeks apart) using MI-Fluid (row 1), MI-Asymmetric Unbiased (row 2), and MI-Symmetric Unbiased (row 3) registration methods. Jacobian maps of deformations from time 2 to time 1 (column 1) and time 1 to time 2 (column 2) are superimposed on the target volumes. The unbiased methods generate less noisy Jacobian maps with values closer to 1; this shows the greater stability of the approach when no volumetric change is present. Column 3 examines the inverse consistency of deformation models. Products of Jacobian maps generated using all three models are shown, for the forward direction (time 1 to time 2) and backward direction (time 2 to time 1). For the mutual information-based unbiased methods, the products of the Jacobian maps are less noisy, with values closer to 1, showing better inverse consistency.

Given the force field, the most straightforward way to minimize (6) might seem to involve parameterizing the descent direction by an artificial time τ,

$$\frac{\partial \mathbf{u}(\mathbf{x},\tau)}{\partial \tau} = -\mathbf{f}(\mathbf{x},\mathbf{u}(\mathbf{x},\tau)). \tag{21}$$

However, in our case, we do not solve Euler-Lagrange equations using the gradient descent method. In order to regularize the flow, we employ the fluid regularization proposed in [6]. Given the velocity field $\mathbf{v}$, the following partial differential equation can be solved to obtain the displacement field $\mathbf{u}$:

$$\frac{\partial \mathbf{u}}{\partial \tau} = \mathbf{v} - \mathbf{v} \cdot \nabla \mathbf{u}. \tag{22}$$

The instantaneous velocity as in [25] is obtained by convolving $\mathbf{f}$ with Gaussian kernel G_σ of variance σ^2:

$$\mathbf{v} = G_\sigma * (-\mathbf{f}(\mathbf{x},\mathbf{u})). \tag{23}$$

This equation can be solved efficiently using the Fast Fourier transform (FFT).

To avoid possible confusion, we summarize the methods we will be referring to in our subsequent analyses.

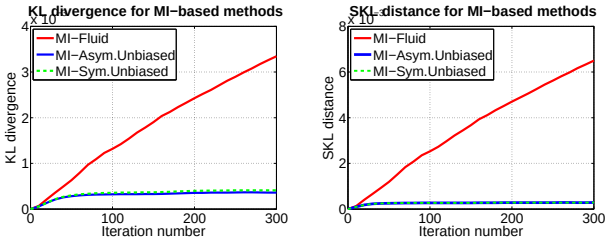

(a) KL divergence (b) SKL distance

Fig. 5 (a) KL divergence and (b) SKL distance per iteration are shown for the MI-Fluid (solid red), MI-Asymmetric Unbiased (solid blue), and MI-Symmetric Unbiased (dashed green) methods. For MI-Fluid, both KL and SKL measures increase. Even though the Asymmetric Unbiased method explicitly minimizes the KL distance, and the Symmetric Unbiased model minimizes the SKL distance, both the KL and SKL measures stabilize for both unbiased methods.

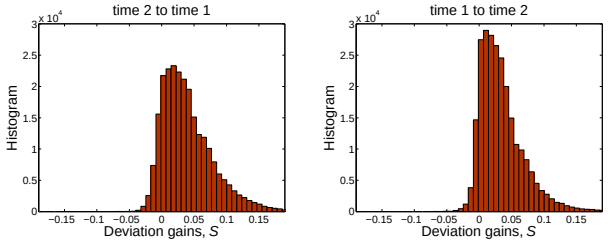

(a) MI-Fluid vs. MI-Asym.Unbiased

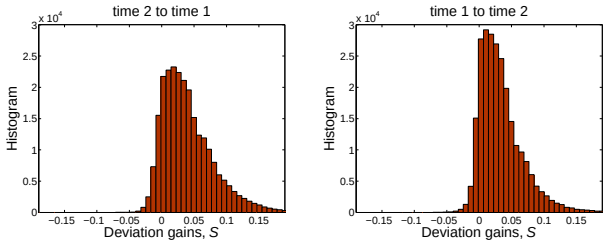

(b) MI-Fluid vs. MI-Sym.Unbiased

Fig. 6 Histograms of voxel-wise deviation gains (a) MI-Fluid over MI-Asymmetric Unbiased and (b) MI-Fluid over MI-Symmetric Unbiased for one of the subjects, for the forward direction (time 2 to time 1) and backward direction (time 1 to time 2). The histograms are skewed to the right, indicating the superiority of Asymmetric Unbiased and Symmetric Unbiased registration methods over Fluid registration. Paired t test shows significance ($p < 0.0001$).

In later discussions, minimization of the following energies

$$E(I_1, I_2, \mathbf{u}) = F_{L^2}(I_1, I_2, \mathbf{u}) + \lambda R_{KL}(\mathbf{u}) \tag{24}$$

and

$$E(I_1, I_2, \mathbf{u}) = F_{L^2}(I_1, I_2, \mathbf{u}) + \lambda R_{SKL}(\mathbf{u}) \tag{25}$$

using equations (20), (23), (22) will be referred to as L^2-Asymmetric Unbiased and L^2-Symmetric Unbiased models, respectively. The model above, provided $\lambda = 0$, will be referred to as the L^2-Fluid model.

Similarly, minimization of

$$E(I_1, I_2, \mathbf{u}) = F_{MI}(I_1, I_2, \mathbf{u}) + \lambda R_{KL}(\mathbf{u}) \tag{26}$$

and

$$E(I_1, I_2, \mathbf{u}) = F_{MI}(I_1, I_2, \mathbf{u}) + \lambda R_{SKL}(\mathbf{u}) \tag{27}$$

will be referred to as the MI-Asymmetric Unbiased and MI-Symmetric Unbiased models, respectively. Such models, with $\lambda = 0$, define the MI-Fluid model.

5 Statistical Analysis

5.1 Statistical testing on the deviation of log Jacobian maps in the absence of changes

Based on the authors' approach in [14], we observe that, given that there is no systematic structural change within two weeks, any deviation of the Jacobian map from one should be considered error. Thus, we expect that a better registration technique would yield $\log|D\mathbf{g}|$ values closer to 0 (i.e., smaller log Jacobian deviation translates into better methodology). Mathematically speaking, one way to test the performance is to consider the deviation map dev of the logged (i.e., logarithmically transformed) Jacobian away from zero, defined at each voxel as

$$dev(\mathbf{x}) = \big|\log|D\mathbf{g}(\mathbf{x})|\big|. \tag{28}$$

For two different registration methods A and B, we define the voxel-wise deviation gain of A over B (denoted by $S^{A,B}$) as

$$S^{A,B}(\mathbf{x}) = dev^A(\mathbf{x}) - dev^B(\mathbf{x}). \tag{29}$$

For the ADNI baseline dataset (in which patients are scanned twice with MRI, two weeks apart), two distinct types of t tests are used, a within-subject paired t test and a group paired t test. A within-subject paired t test is conducted for each subject by pooling all voxels inside a region of interest, as defined by the ICBM whole brain mask (the ICBM brain is a standardized population average image, defined by the International Consortium for Brain Mapping [26]). This determines whether two methods differ significantly inside the whole brain (for each subject). A group paired t test, on the other hand, is performed across subjects, by computing a voxel-wise t-map of deviation gains. In this case, to statistically compare the performance of two registration methods, we rely on the standard t test on the voxel mean of S. To construct a suitable null hypothesis, we notice that the following relation would hold, assuming B outperforms A

$$S^{A,B} > 0. \tag{30}$$

Thus, the null hypothesis in this case would be testing if the mean deviation gain is zero

$$H_0 : \mu_{S^{A,B}} = 0. \tag{31}$$

To determine the ranking of A and B, we have to consider one-sided alternative hypotheses. For example, when testing if B outperforms A, we use the following alternative hypothesis

$$H_1 : \mu_{S^{A,B}} > 0. \tag{32}$$

The voxel-wise T statistic, defined as

$$T_{S^{A,B}}(\mathbf{x}) = \frac{\sqrt{n} \cdot \overline{S^{A,B}(\mathbf{x})}}{\sigma_{S^{A,B}}(\mathbf{x})}, \tag{33}$$

where

$$\overline{S^{A,B}(\mathbf{x})} = \frac{\sum_i S_i^{A,B}(\mathbf{x})}{n}, \tag{34}$$

and

$$\left(\sigma_{S^{A,B}}(\mathbf{x})\right)^2 = \frac{\sum_i \left(S_i^{A,B}(\mathbf{x}) - \overline{S^{A,B}(\mathbf{x})}\right)^2}{n-1}, \tag{35}$$

thus follows the Student's t distribution under the null hypothesis and may be used to determine the p-value that the null hypothesis is true. If the alternative hypothesis is accepted, we confirm that sequence B outperforms A at point $\mathbf{x}$. Otherwise, we would rank A and B equally if the null hypothesis is not rejected.

5.2 Detecting Real Changes - Statistical testing on the mean log Jacobian

For both the ADNI follow-up dataset (in which patients are scanned twice with MRI, one year apart) and ADNI baseline dataset, we create a voxel-wise t map using the local log Jacobian values of the ten subjects, allowing us to test the validity of the zero mean assumption. To simplify the notation, we introduce J to denote $J = |D\mathbf{g}|$. The following voxel-wise T statistic compared to a two-tailed Student's t distribution may then be used to test the above null hypothesis

$$T_{\log J}(\mathbf{x}) = \frac{\sqrt{n} \cdot \overline{\log J(\mathbf{x})}}{\sigma_{\log J}(\mathbf{x})}, \tag{36}$$

where

$$\overline{\log J(\mathbf{x})} = \frac{\sum_i \log J_i(\mathbf{x})}{n}, \tag{37}$$

and

$$\left(\sigma_{\log J}(\mathbf{x})\right)^2 = \frac{\sum_i \left(\log J_i(\mathbf{x}) - \overline{\log J(\mathbf{x})}\right)^2}{n-1}. \tag{38}$$

We reject the null hypothesis if the p value calculated above exceeds a pre-set threshold based on a suitable confidence interval. Notice the voxel-wise variance of $\log J$ provides us with a way to assess the repeatability of a deformation method, i.e., measuring the voxel-wise spread of the given multiple observations (with higher variance corresponding to lower repeatability).

5.3 Permutation Testing to Correct Multiple Comparisons

To determine the overall global effects of different registration methods on the deviation of log Jacobian maps throughout the brain, we performed permutation tests to adjust for multiple comparisons [27,28]. Following the analyses in [16], we resampled the observations by randomly flipping the sign of $S_i^{A,B}$ $(i = 1, 2, ..., n)$ under the null hypothesis. For each permutation, voxel-wise t tests are computed. We then compute the percentage of voxels inside the chosen ROI (in this case the ICBM mask) with T statistics exceeding a certain threshold. The multiple comparisons corrected p value may be determined by counting the number of permutations whose above-defined percentage exceeds that of the un-permuted observed data. This is comparable to 'set-level inference' in the widely-used SPM (Statistical Parametric Mapping) functional image analysis package [29]. For example, we say that sequence B outperforms A on the whole brain if this corrected p value is smaller than 0.05 (that is, less than 5% of all permutations have the above-defined percentage greater than that of the original data). All possible ($2^{10} = 1024$) permutations were considered in determining the final corrected p value.

5.4 Cumulative Distribution Function (CDF)

To visually assess the global significance level of the voxel-wise t tests on deviation gains and log-Jacobian values, we also employed the cumulative distribution function (CDF) plot, as in several prior studies [30–33]. In brief, we plot observed cumulative probabilities against the theoretical distribution under the null hypothesis. These CDF plots are commonly created as an intermediate step, when using the false discovery rate (FDR) method to assign overall significance values to statistical maps [34–37]. As they show the proportion of supra-threshold voxels in a statistical map, for a range of thresholds, these CDF plots (sometimes called Q-Q plots) offer a measure of the effect size in a statistical map. They also may be used to demonstrate

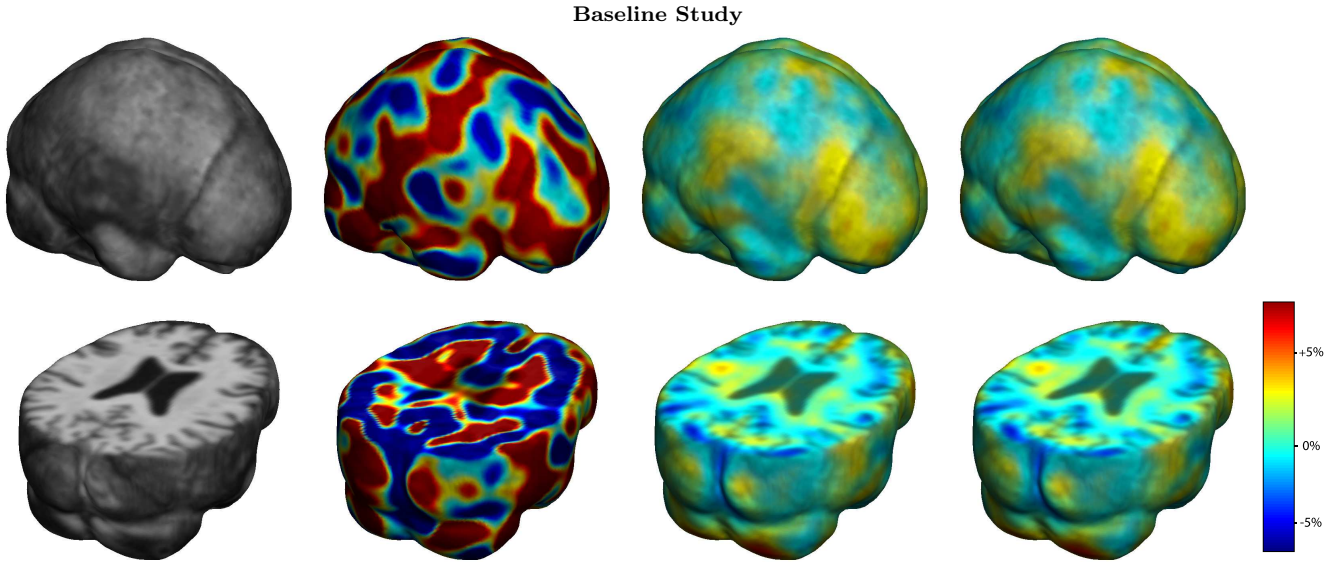

(a) Volume (b) L^2-Fluid (c) L^2-Asym.Unbiased (d) L^2-Sym.Unbiased

Fig. 7 Nonrigid registration was performed on the ADNI Baseline study (serial MRI images acquired two weeks apart) of ten normal elderly subjects using L^2-Fluid (column 2), L^2-Asymmetric Unbiased (column 3), L^2-Symmetric Unbiased (column 4) registration methods. For each method, the mean of the resulting 10 Jacobian maps is superimposed on one of the brain volumes. Visually, L^2-Fluid generates a noisy mean map, while maps generated using L^2-Asymmetric Unbiased and L^2-Symmetric Unbiased methods are less noisy with values closer to 1. For all deformation models, regions with least stability, due to both spatial distortion and intensity inhomogeneity, are the brain stem, thalamus, and ventricles.

Table 1 Global T statistics for all ten subjects testing whether Symmetric Unbiased registration (method B) outperforms Fluid registration (method A) when coupled with L^2.

Subject #	1	2	3	4	5	6	7	8	9	10
$\overline{S^{A,B}}$	0.0639	0.0337	0.0758	0.101	0.0968	0.0581	0.473	0.583	0.288	0.238
$\sigma^2_{S^{A,B}}$	0.00342	0.00102	0.00567	0.00906	0.00926	0.00416	0.185	0.386	0.0618	0.0515
$T_{S^{A,B}}$	542	524	499	525	499	447	546	465	575	520

Table 2 Global T statistics for all ten subjects testing whether Symmetric Unbiased registration (method B) outperforms Fluid registration (method A) when coupled with mutual information.

Subject #	1	2	3	4	5	6	7	8	9	10
$\overline{S^{A,B}}$	0.0697	0.0262	0.0399	0.0342	0.0379	0.0820	0.0853	0.0774	0.0489	0.0773
$\sigma^2_{S^{A,B}}$	0.00579	0.000774	0.00156	0.00138	0.00138	0.00708	0.00845	0.00698	0.00232	0.00529
$T_{S^{A,B}}$	455	468	501	456	505	484	460	460	504	527

which methodological choices influence the effect size in a method that creates statistical maps [30,32,31].

In the case of deviation gains S of a worse technique A over a better technique B in the ADNI baseline data, we expect a CDF curve to lie above the Null line, in the sense that a better technique exhibits less systematic changes. In the case of log-Jacobian values, a better registration technique, on the other hand, should be able to separate the CDF curves between ADNI baseline and follow-up phases (this is what we refer to as the separation of CDF curves in the presence of real physiological changes).

6 Results

In this section, we tested the Asymmetric Unbiased and Symmetric Unbiased models and compared the results to those obtained using the Fluid registration model [6, 25]. Of note, even though Asymmetric Unbiased and Symmetric Unbiased methods minimize different energy functionals, our experiments showed that they generate very similar maps. For each regularization technique, we employed both L^2 and mutual information matching functionals (see equations (24)-(27)).

To obtain a fair comparison, re-gridding was not employed. Re-gridding is a method to relax the energy computed from the linear elasticity prior after a certain number of iterations, which allows large-deformation mappings to be recovered without any absolute penalty on the displacement field (other than via the smoothness constraint on the velocity field which is integrated to give the displacement) [6]. It is essentially a memoryless procedure, as how images are matched after each re-gridding is independent of the final deformation before the re-gridding, rendering the comparison of final Jacobian fields and cost functionals problematic. Moreover, we consider the strategy of re-gridding, through the relaxation of deformation fields over time, to be less rigorous from a theoretical standpoint, as the imposition of a regularizer can be used to secure distributional properties in the resulting statistics (e.g., symmetric log-Jacobian).

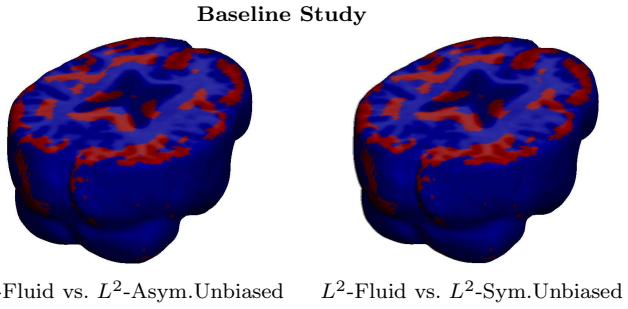

Fig. 8 Voxel-wise paired t test for the deviation gain S empirically thresholded at 2.82 ($p = 0.005$ on the voxel level with 9 degrees of freedom), showing where L^2-Asymmetric Unbiased and L^2-Symmetric Unbiased registration outperform L^2-Fluid registration (regions in red) with statistical significance on a voxel level. In contrast, there are no voxels with T values smaller than -2.82, indicating that Fluid registration does not outperform unbiased methods at any voxel. Hence, the visualization of voxel-wise paired t test with a threshold of -2.82 is omitted.

6.1 ADNI Baseline Scans

In this section, nonlinear registration was performed on a dataset that we shall refer to as the "ADNI Baseline" dataset, collected during the preparatory phase of the ADNI project, which includes serial MRI images of ten normal elderly subjects acquired two weeks apart. Each of the ten pairs of scans is represented on a $128 \times 160 \times 128$ grid. Here, the foundation of calibrations is based on the assumption that, by scanning normal control human subjects serially within a two-week period using the same MRI protocol, no systematic structural changes should be recovered.

In our first experiment, we compared methods based on L^2 matching (L^2-Fluid, L^2-Asymmetric Unbiased, and L^2-Symmetric Unbiased). Uniform values of $\lambda = 500$ and $\lambda = 1000$ were used for all deformations using L^2-Symmetric Unbiased and L^2-Asymmetric Unbiased algorithms, respectively. Since the Asymmetric Unbiased model quantifies only the forward deformation, the weight of the corresponding regularization functional is half the magnitude of that of the Symmetric Unbiased model, and hence, a weighting parameter twice as large should be used.

Figures 1-3 show the results of registering a pair of serial MRI images for one of the subjects (subject 3). The deformation was computed in both directions (time 2 to time 1, and time 1 to time 2) using methods based on L^2 matching. In Figure 1, Jacobian maps of deformations are superimposed on brain volumes. Both Asymmetric Unbiased and Symmetric Unbiased methods generate less noisy Jacobian maps with values closer to the identity mapping, which shows the superior stability of the Unbiased approach in the absence of physiological changes. We also visually assessed the *inverse consistency* of the mappings [38] by concatenating forward and backward Jacobian maps (in an ideal situation, this operation should yield the identity). Again, we observe noticeable visual differences between the results obtained using the unbiased methods and Fluid registration. Figure 2 plots the KL divergence and SKL distance measures for each of the L^2-based methods. For L^2-Fluid method, both KL and SKL measures increase with increasing numbers of iterations. On the other hand, even though the Asymmetric Unbiased method minimizes the KL divergence and the Symmetric Unbiased model minimizes the SKL distance, these two measures stabilize for both unbiased methods. Figure 3 shows the histograms of voxel-wise deviation gains of L^2-Fluid over L^2-Asymmetric Unbiased as well as L^2-Fluid over L^2-Symmetric Unbiased. The histograms are skewed to the right, indicating the superiority of both unbiased registration methods over Fluid registration.

Of note, we have also considered a different deviation map, defined as $dev_2(\mathbf{x}) = \big||D\mathbf{g}(\mathbf{x})| - 1\big|$, in place of (28). We performed statistical analyses with this definition of deviation gain, which yielded very similar results. These results are therefore not shown in this paper.

In Table 1, we compared L^2-Fluid and L^2-Symmetric Unbiased methods, conducting a within-subject paired t test inside the ICBM mask for each of the ten subjects. In this case, $p < 0.0001$ for all subjects, indicating that the Symmetric Unbiased registration, when coupled with L^2 matching cost functional, produces more reproducible maps with less variability.

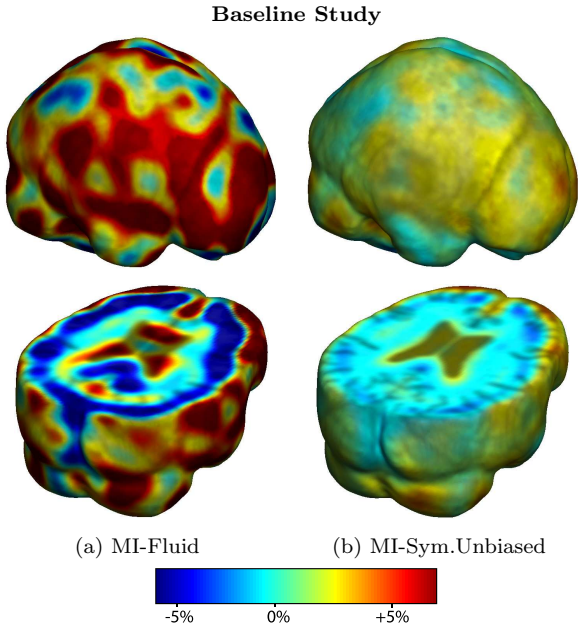

Fig. 9 Nonrigid registration was performed on the ADNI Baseline study (serial MRI images acquired two weeks apart) of ten normal elderly subjects using MI-Fluid (column 1) and MI-Symmetric Unbiased (column 2) registration methods. For each method, the mean of the resulting 10 Jacobian maps is superimposed on one of the brain volumes. Visually, MI-Fluid generates a noisy mean map, while map generated using MI-Symmetric Unbiased method is less noisy with values closer to 1. For both deformation models, regions with least stability, due to both spatial distortion and intensity inhomogeneity, are the brain stem, thalamus, and ventricles. The results obtained using MI-Asymmetric Unbiased method are similar to those obtained using MI-Symmetric Unbiased method, and are therefore omitted.

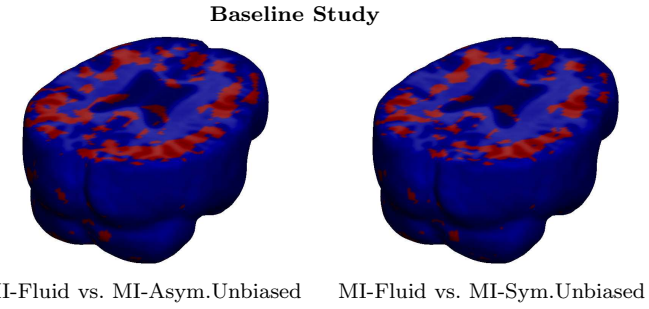

Fig. 10 Voxel-wise paired t test for the deviation gain S empirically thresholded at 2.82 ($p = 0.005$ on the voxel level with 9 degrees of freedom), showing where MI-Asymmetric Unbiased and MI-Symmetric Unbiased registration outperform MI-Fluid registration (regions in red) with statistical significance on a voxel level. In contrast, there are no voxels with T values smaller than -2.82, indicating that Fluid registration does not outperform unbiased methods at any voxel. Hence, the visualization of voxel-wise paired t test with a threshold of -2.82 is omitted.

Figure 7 shows the mean Jacobian maps obtained using L^2-Fluid, L^2-Asymmetric Unbiased, and L^2- Symmetric Unbiased registration algorithms. Jacobian maps generated using unbiased models have values closer to 1, whereas L^2-Fluid model generated noisy mean maps. Figure 8, shows the results when performing 3D voxel-wise paired t tests for the deviation gain of L^2-Fluid over L^2-Asymmetric Unbiased and L^2-Fluid over L^2-Symmetric Unbiased. T maps for the deviation gains are empirically thresholded at 2.28 ($p = 0.005$ on the voxel level with 9 degrees of freedom) to show statistical significance.

Figure 11(a) shows results obtained using Multiple Comparison Analysis using permutation testing on deviation gains of L^2-Fluid over L^2-Symmetric Unbiased. The results indicate that out of 1024 permutations, no permutation yields a larger percentage of voxels with $p < 0.05$ than the observed data, which indicates that L^2-Symmetric Unbiased method outperforms L^2-Fluid with $p < 0.001$.

To emphasize the differences between the distributions of log Jacobian values for Fluid and unbiased (both asymmetric and symmetric) methods, in Figure 12, we plotted the cumulative distribution function of the p-values in deviation gains as defined in (29). In these plots, the interval $p \in [0, 0.05]$ is the most important. For a null distribution, this cumulative plot falls along the line $y = x$ in xy-plane, as represented by the dashed black line. Larger upward inflections of the CDF curve near the origin are associated with significant deviation gains, indicating that both Asymmetric Unbiased and Symmetric Unbiased methods outperform Fluid method in being less likely to exhibit structural changes in the absence of systematic biological changes.

In our second experiment, we compared the performance of methods based on mutual information matching (MI-Fluid, MI-Asymmetric Unbiased, and MI- Symmetric Unbiased). As for methods based on L^2 matching, Figures 4-6 demonstrate MI-Asymmetric Unbiased and MI-Symmetric Unbiased methods to produce inverse consistent maps with less variability. Table 2 shows the results of within-subject paired t test for all ten subjects. The results, based on mean Jacobian maps for all subjects, show that the Unbiased regularization technique outperforms Fluid registration with confirmed statistical significance (Figures 9, 10, 11(b), and 13).

Lastly, we compared L^2 and mutual information cost functionals for both Fluid and Symmetric Unbiased regularization. (Since Asymmetric Unbiased and Symmetric Unbiased regularizations produce similar results, we do not show the results for the asymmetric version). We again conducted within-subject paired t tests (Tables 3 and 4) as well as group paired t tests (Figure 14) on the voxel-wise deviation gains for all

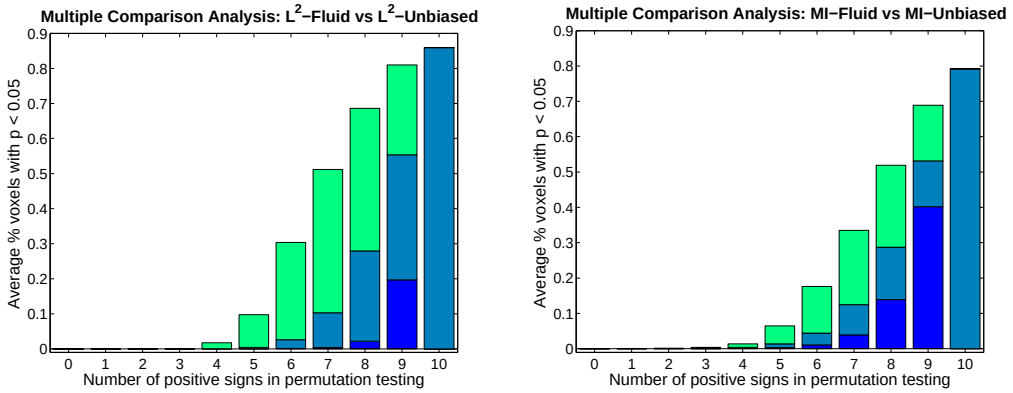

(a) L^2-Fluid vs. L^2-Symmetric Unbiased (b) MI-Fluid vs. MI-Symmetric Unbiased

Fig. 11 Multiple Comparison Analysis using permutation testing on the deviation gain S of (a) L^2-Fluid over L^2-Symmetric Unbiased and (b) MI-Fluid over MI-Symmetric Unbiased, both for baseline ADNI dataset. Each permutation randomly assigns a positive or negative sign to each of the 10 log-Jacobian maps. Here, results are plotted with respect to the number of positive signs (from 0 to 10) with 10 positive signs indicating the observed data. Dark blue, light blue, and green colors indicate the minimum, average, and maximum percentage of voxels with $p < 0.05$ of all possible permutations with a given number of positive signs. There is only one observation for the observed data, and thus, minimum, maximum, and average values are equal for the rightmost bar. The result indicates that out of 1024 permutations, no permutation gives a greater percentage of voxels with $p < 0.05$ than the observed data does. This indicates that unbiased regularization technique outperforms Fluid methods with $p < 0.001$. Since the results obtained using Asymmetric Unbiased method are similar to those obtained using Symmetric Unbiased method, they are not shown here.

voxels inside the ICBM brain mask. We showed that MI-Fluid outperforms L^2-Fluid with $p < 0.0001$. However, the result of the comparison of L^2-Symmetric Unbiased and MI-Symmetric Unbiased is inconclusive. In other words, mutual information performs better when coupled with Fluid registration, but there is no statistical difference between mutual information and L^2 when the Symmetric Unbiased method is used.

To explain this result, we postulate that by constraining the deformations less (i.e., as in Fluid registration), assuming intensity 1-to-1 correspondence (i.e., matching using L^2) may lead to local oscillations of the deformation maps, as minimizing L^2 forces a local search for the smallest intensity differences. One result of this is a Jacobian map with locally extreme values, translating into spurious signals and, in our case, less reproducibility. On the other hand, the Symmetric Unbiased method eliminates local oscillations, allowing globally better matching when intensity 1-to-1 correspondence can be assumed (i.e., when L^2 is applicable as a data fidelity term).

6.2 ADNI Follow-up Scans

In this section, we analyze a dataset we shall call the "ADNI Follow-up" phase dataset, which includes serial MRI images ($220 \times 220 \times 220$) of ten subjects acquired one year apart. These data were collected as part of a larger study to track degenerative brain changes in MRI in 800 subjects, ages 55 to 90, including 200 elderly controls, 400 subjects with mild cognitive impairment, and 200 patients with AD. As the images are now one year apart, real anatomical changes are present, which allows methods to be compared in the presence of true biological changes.

In Figure 15, nonlinear registration was performed using Fluid, Asymmetric Unbiased, and Symmetric Unbiased methods coupled with L^2 matching. Visually, the Fluid method generates noisy mean Jacobian maps, while maps generated using unbiased methods suggest a volume reduction in gray matter as well as ventricular enlargement. Here, both Asymmetric Unbiased and Symmetric Unbiased methods perform equally well. Figure 17 displays the cumulative distribution of p-values for the voxel-wise log Jacobian t-maps for both ADNI Baseline and ADNI Follow-up datasets. We expect a better method to separate these two CDF curves, indicating that a real biological change has occurred between the two time points. A greater separation is accomplished when Asymmetric Unbiased and Symmetric Unbiased methods are used, while the Fluid method does not differentiate between the two datasets. Similar results are obtained using mutual information based methods (Figure 16).

7 Conclusion

This paper introduced a novel asymmetric unbiased registration model (the Asymmetric Unbiased model), which produces results that are very similar to those ob-

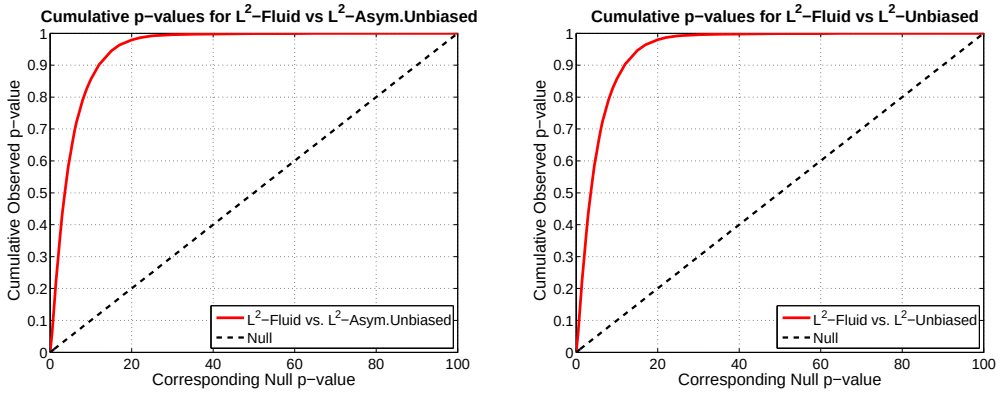

(a) L^2-Fluid vs. L^2-Asym.Unbiased (b) L^2-Fluid vs. L^2-Sym.Unbiased

Fig. 12 Cumulative distribution of p-values for the deviation gain S of (a) L^2-Fluid over L^2-Asymmetric Unbiased and (b) L^2-Fluid over L^2-Symmetric Unbiased. Here, the ADNI baseline dataset is used. In both (a) and (b), the CDF line is well above the Null line ($y = x$), indicating that both asymmetric and symmetric unbiased methods outperform Fluid method (i.e. less deviation) in being less likely to exhibit structural change in the absence of biological change. Note that the interval $p \in [0, 0.05]$ is of most importance for observation.

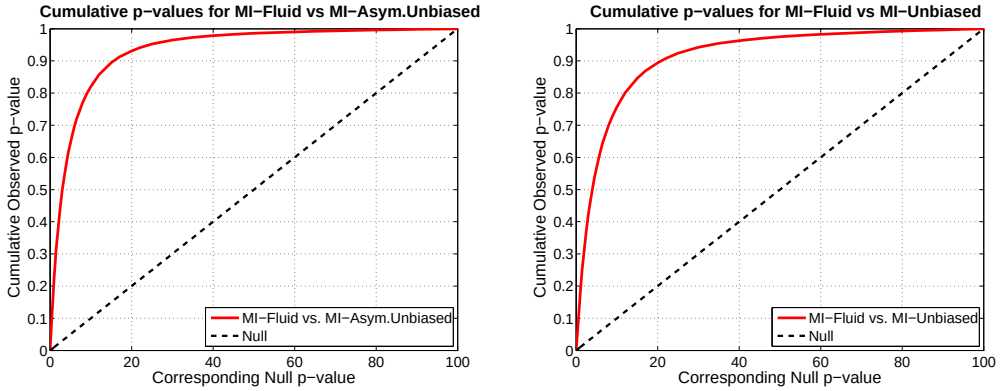

(a) MI-Fluid vs. MI-Asym.Unbiased (b) MI-Fluid vs. MI-Sym.Unbiased

Fig. 13 Cumulative distribution of p-values for the deviation gain S of (a) MI-Fluid over MI-Asymmetric Unbiased and (b) MI-Fluid over MI-Symmetric Unbiased. Here, ADNI baseline dataset is used. In both (a) and (b), the CDF line is well above the Null line, indicating that both asymmetric and symmetric unbiased methods outperform Fluid method in being less likely to exhibit structural change in the absence of biological change. Note that the interval $p \in [0, 0.05]$ is of most importance for observation.

Table 3 Global T statistics for all ten subjects testing whether MI-Fluid (method B) outperforms L^2-Fluid (method A).

Subject #	1	2	3	4	5	6	7	8	9	10
$\overline{S^{A,B}}$	0.000997	0.00435	0.0520	0.0971	0.0721	0.0269	0.445	0.566	0.274	0.196
$\sigma^2_{S^{A,B}}$	0.00819	0.00121	0.00529	0.0156	0.0118	0.00406	0.190	0.372	0.0694	0.0457
$T_{S^{A,B}}$	5	62	355	385	329	210	506	461	516	454

tained using the previously introduced Symmetric Unbiased model. This work has also, for the first time, analyzed unbiased models with mutual information based matching functionals. It is the first paper to systematically investigate the reproducibility and variability of different registration methods in TBM. We showed that Asymmetric Unbiased and Symmetric Unbiased models perform significantly better than the fluid registration technique. When applied to serial scans obtained using the same protocol, inconclusive results are obtained when comparing the stability of L^2-Unbiased and MI-Unbiased (both asymmetric and symmetric) models. However, L^2-Fluid performs less favorably than MI-Fluid. Although various techniques have been extensively applied to detect disease effects and monitor brain changes with TBM, this paper is the first calibration study to compare registration models for tensor-based morphometry. We believe our results are impor-

Table 4 Global T statistics for all ten subjects testing whether L^2-Symmetric Unbiased (method B) outperforms MI-Symmetric Unbiased (method A).

Subject #	1	2	3	4	5	6	7	8	9	10
$\overline{S^{A,B}}$	0.00648	0.00314	-0.0161	-0.0244	-0.0132	0.0101	-0.0568	-0.0746	-0.0352	-0.0347
$\sigma^2_{S^{A,B}}$	0.000458	0.000111	0.000424	0.00155	0.000593	0.000262	0.00323	0.00367	0.00133	0.00121
$T_{S^{A,B}}$	150	148	-387	-307	-269	309	-497	-611	-478	-495

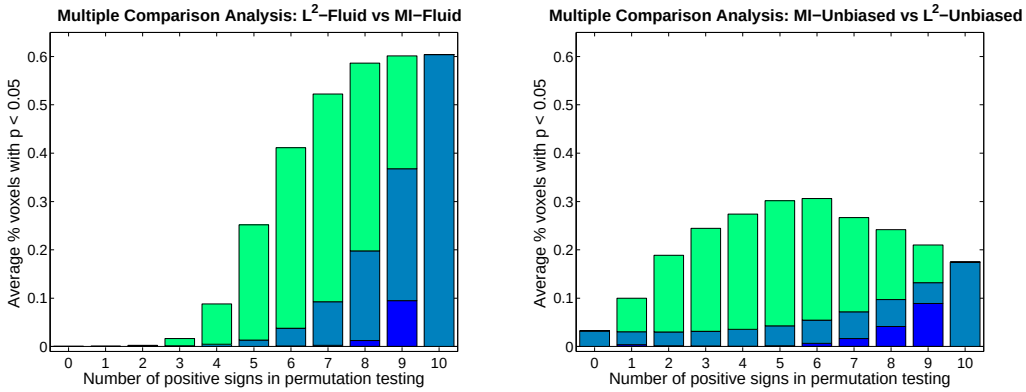

(a) L^2-Fluid vs. MI-Fluid (b) MI-Sym.Unbiased vs. L^2-Sym.Unbiased

Fig. 14 Multiple Comparison Analysis using permutation testing on the deviation gain S of (a) L^2-Fluid over MI-Fluid and (b) MI-Symmetric Unbiased over L^2-Symmetric Unbiased, both for baseline ADNI dataset. Each permutation randomly assigns positive or negative sign to each of the 10 log-Jacobian maps. Here, results are plotted with respect to the number of positive signs (from 0 to 10) with 10 positive signs indicating the observed data. Dark blue, light blue, and green colors indicate the minimum, average, and maximum percentage of voxels with $p < 0.05$ of all possible permutations with a given number of positive signs. There is only one observation for the observed data, and thus, minimum, maximum, and average values are equal for the rightmost bar. The result in (a) indicates that out of 1024 permutations, no permutation gives a greater percentage of voxels with $p < 0.05$ than the observed data does. This indicates that MI-Fluid method outperforms L^2-Fluid method with $p < 0.001$. However, the comparison of MI-Symmetric Unbiased and L^2-Symmetric Unbiased in (b) is inconclusive. Since the results obtained using Asymmetric Unbiased method are similar to those obtained using Symmetric Unbiased method, they are not shown here.

tant, as they provide greater insight into the interpretation of TBM results in the future.

A Derivations of Gradient of $R(\mathbf{u})$ in Two Spatial Dimensions

In this Appendix, we derive explicit expressions for $\partial_{\mathbf{u}} R(\mathbf{u})$ in (20) when $\Omega \subset \mathbb{R}^2$. Let us denote the components of vector $\mathbf{x}$ to be (x_1, x_2) and the components of vector $\mathbf{u}$ be (u_1, u_2). We also denote $\partial_j u_i = \partial u_i / \partial x_j$.

To simplify the notation, we let $J = |D\mathbf{g}| = |D(\mathbf{x} - \mathbf{u})|$. Also, denote $L(J) = L_{KL}(J) = -\log J$, when $R = R_{KL}$ and $L(J) = L_{SKL}(J) = (J-1)\log J$, when $R = R_{SKL}$. Note that $J : \mathcal{M}_{2\times 2}(\mathbb{R}) \to \mathbb{R}$, where $\mathcal{M}_{2\times 2}(\mathbb{R})$ is the set of 2×2 matrices with real elements, and $L : \mathbb{R} \to \mathbb{R}$. Jacobian J is a function of $\partial_j u_i$, for $i, j = 1, 2$, and is given by

$$J\big(\partial_1 u_1, \partial_2 u_1, \partial_1 u_2, \partial_2 u_2\big) = (1 - \partial_1 u_1)(1 - \partial_2 u_2) - \partial_2 u_1\, \partial_1 u_2.$$

We would like to minimize the functional

$$R(\mathbf{u}) = \int_\Omega L\big(\partial_1 u_1, \partial_2 u_1, \partial_1 u_2, \partial_2 u_2\big) d\mathbf{x}.$$

We find the first Euler-Lagrange equation. For some $\eta \in C_c^1(\Omega)$:

$$\begin{aligned} &\frac{dR}{d\varepsilon}(u_1 + \varepsilon\eta, u_2)\big|_{\varepsilon=0} \\ &= \int_\Omega \left[\frac{dL}{dJ}\frac{\partial J}{\partial(\partial_1 u_1)}\,\partial_{x_1}\eta + \frac{dL}{dJ}\frac{\partial J}{\partial(\partial_2 u_1)}\,\partial_{x_2}\eta\right] d\mathbf{x} \\ &= -\int_\Omega \left[\frac{\partial}{\partial x_1}\left(\frac{dL}{dJ}\frac{\partial J}{\partial(\partial_1 u_1)}\right) + \frac{\partial}{\partial x_2}\left(\frac{dL}{dJ}\frac{\partial J}{\partial(\partial_2 u_1)}\right)\right]\eta\, d\mathbf{x}. \end{aligned} \tag{39}$$

With notation $L' = dL/dJ$, the first Euler-Lagrange equation becomes:

$$-\frac{\partial}{\partial x_1}\left(L'\frac{\partial J}{\partial(\partial_1 u_1)}\right) - \frac{\partial}{\partial x_2}\left(L'\frac{\partial J}{\partial(\partial_2 u_1)}\right) = 0. \tag{40}$$

Thus, minimizing the energy $R(\mathbf{u})$ with respect to u_1, for fixed u_2, yields the first component of $\partial_{\mathbf{u}} R(\mathbf{u})$:

$$\partial_{u_1} R(\mathbf{u}) = \frac{\partial}{\partial x_1}\Big((1 - \partial_2 u_2)L'\Big) + \frac{\partial}{\partial x_2}\Big(\partial_1 u_2\, L'\Big). \tag{41}$$

Note that $L'_{KL}(J) = -1/J$ and $L'_{SKL}(J) = 1 + \log J - 1/J$. Similarly, the Euler-Lagrange equation for the second component of $\partial_{\mathbf{u}} R(\mathbf{u})$ can be found to be:

$$\partial_{u_2} R(\mathbf{u}) = \frac{\partial}{\partial x_1}\Big(\partial_2 u_1\, L'\Big) + \frac{\partial}{\partial x_2}\Big((1 - \partial_1 u_1)L'\Big). \tag{42}$$

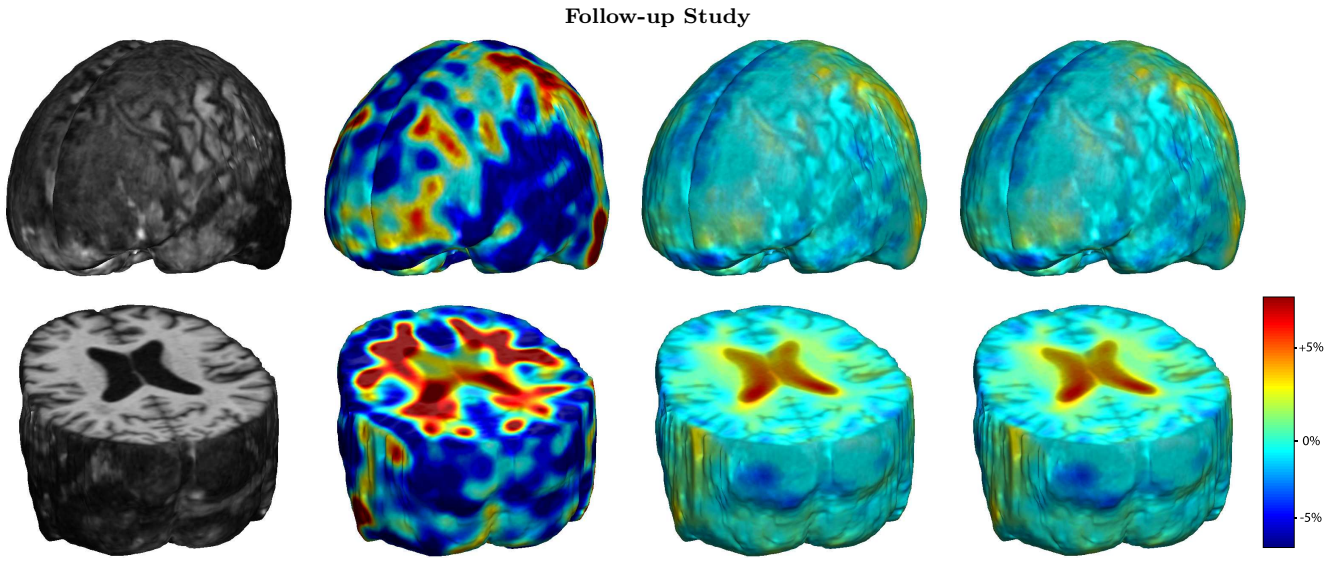

(a) Volume (b) L^2-Fluid (c) L^2-Asym.Unbiased (d) L^2-Sym.Unbiased

Fig. 15 Nonrigid registration was performed on the ADNI Follow-up study (serial MRI images acquired 12 months apart) using L^2-Fluid (column 2), L^2-Asymmetric Unbiased (column 3), and L^2-Symmetric Unbiased (column 4) registration methods. For each method, the mean of the resulting 10 Jacobian maps is superimposed on one of the brain volumes. Visually, L^2-Fluid generates a noisy mean map, while maps generated using the L^2-Asymmetric Unbiased and L^2-Symmetric Unbiased methods suggest a volume reduction in gray matter as well as ventricular enlargement.

B Derivations of Gradient of $R(\mathbf{u})$ in Three Spatial Dimensions

In this Appendix, we derive an explicit expression for $\partial_{\mathbf{u}} R(\mathbf{u})$ in (20) when $\Omega \subset \mathbb{R}^3$. Let us denote the components of vector $\mathbf{x}$ to be (x_1, x_2, x_3) and the components of vector $\mathbf{u}$ be (u_1, u_2, u_3). Here, we will use the same notation we used in Appendix A.

Jacobian J is a function of $\partial_j u_i$, for $i, j = 1, 2, 3$, and is given by

$$\begin{aligned} &J\big(\partial_1 u_1, \partial_2 u_1, \partial_3 u_1, \partial_1 u_2, \partial_2 u_2, \partial_3 u_2, \partial_1 u_3, \partial_2 u_3, \partial_3 u_3\big) \\ &= (1-\partial_1 u_1)(1-\partial_2 u_2)(1-\partial_3 u_3) \;-\; \partial_1 u_2\, \partial_2 u_3\, \partial_3 u_1 \\ &\quad - \partial_2 u_1\, \partial_3 u_2\, \partial_1 u_3 \;-\; \partial_3 u_1 (1-\partial_2 u_2) \partial_1 u_3 \\ &\quad - \partial_2 u_1\, \partial_1 u_2 (1-\partial_3 u_3) \;-\; \partial_3 u_2\, \partial_2 u_3 (1-\partial_1 u_1). \end{aligned} \tag{43}$$

We would like to minimize the functional

$$R(\mathbf{u}) = \int_\Omega L\big(J(\partial_j u_i)\big) d\mathbf{x}, \quad 1 \le i, j \le 3.$$

For some η, we have

$$\begin{aligned} \frac{dR}{d\varepsilon}(u_1 + \varepsilon\eta, u_2, u_3)\big|_{\varepsilon=0} &= \int_\Omega \left[\frac{dL}{dJ} \frac{\partial J}{\partial(\partial_1 u_1)}\, \partial_{x_1}\eta \right. \\ &\quad \left. + \frac{dL}{dJ} \frac{\partial J}{\partial(\partial_2 u_1)}\, \partial_{x_2}\eta + \frac{dL}{dJ} \frac{\partial J}{\partial(\partial_3 u_1)}\, \partial_{x_3}\eta \right] d\mathbf{x} \\ &= -\int_\Omega \left[\frac{\partial}{\partial x_1}\left(\frac{dL}{dJ} \frac{\partial J}{\partial(\partial_1 u_1)} \right) + \frac{\partial}{\partial x_2}\left(\frac{dL}{dJ} \frac{\partial J}{\partial(\partial_2 u_1)} \right) \right. \\ &\quad \left. + \frac{\partial}{\partial x_3}\left(\frac{dL}{dJ} \frac{\partial J}{\partial(\partial_3 u_1)} \right) \right] \eta\, d\mathbf{x}. \end{aligned} \tag{44}$$

Hence, the first Euler-Lagrange equation becomes:

$$\begin{aligned} &-\frac{\partial}{\partial x_1}\left(L' \frac{\partial J}{\partial(\partial_1 u_1)} \right) - \frac{\partial}{\partial x_2}\left(L' \frac{\partial J}{\partial(\partial_2 u_1)} \right) \\ &\quad - \frac{\partial}{\partial x_3}\left(L' \frac{\partial J}{\partial(\partial_3 u_1)} \right) = 0. \end{aligned} \tag{45}$$

Thus, minimizing the energy $R(\mathbf{u})$ with respect to u_1, for fixed u_2 and u_3, yields the first component of $\partial_{\mathbf{u}} R(\mathbf{u})$:

$$\begin{aligned} \partial_{u_1} R(\mathbf{u}) &= \frac{\partial}{\partial x_1}\Big(\big((1-\partial_2 u_2)(1-\partial_3 u_3) - \partial_3 u_2\, \partial_2 u_3\big) L' \Big) \\ &\quad + \frac{\partial}{\partial x_2}\Big(\big(\partial_3 u_2\, \partial_1 u_3 + \partial_1 u_2 (1-\partial_3 u_3)\big) L' \Big) \\ &\quad + \frac{\partial}{\partial x_3}\Big(\big(\partial_1 u_2\, \partial_2 u_3 + (1-\partial_2 u_2) \partial_1 u_3\big) L' \Big). \end{aligned} \tag{46}$$

Similarly, the other two Euler-Lagrange equations can be found to be:

$$\begin{aligned} \partial_{u_2} R(\mathbf{u}) &= \frac{\partial}{\partial x_1}\Big(\big(\partial_2 u_3\, \partial_3 u_1 + \partial_2 u_1 (1-\partial_3 u_3)\big) L' \Big) \\ &\quad + \frac{\partial}{\partial x_2}\Big(\big((1-\partial_1 u_1)(1-\partial_3 u_3) - \partial_3 u_1\, \partial_1 u_3\big) L' \Big) \\ &\quad + \frac{\partial}{\partial x_3}\Big(\big(\partial_2 u_1\, \partial_1 u_3 + \partial_2 u_3 (1-\partial_1 u_1)\big) L' \Big), \end{aligned} \tag{47}$$

and

$$\begin{aligned} \partial_{u_3} R(\mathbf{u}) &= \frac{\partial}{\partial x_1}\Big(\big(\partial_2 u_1\, \partial_3 u_2 + \partial_3 u_1 (1-\partial_2 u_2)\big) L' \Big) \\ &\quad + \frac{\partial}{\partial x_2}\Big(\big(\partial_1 u_2\, \partial_3 u_1 + \partial_3 u_2 (1-\partial_1 u_1)\big) L' \Big) \\ &\quad + \frac{\partial}{\partial x_3}\Big(\big((1-\partial_1 u_1)(1-\partial_2 u_2) - \partial_2 u_1\, \partial_1 u_2\big) L' \Big). \end{aligned} \tag{48}$$

C Derivation of equations for maximization of Mutual Information

In this Appendix, we derive the gradient $\partial_{\mathbf{u}} F_{MI}(\mathbf{u})$ of the mutual information matching functional in (16), adopting the approach of [23,39], modeling the joint intensity distribution $p^{I_1,I_2}_{\mathbf{u}+\varepsilon\boldsymbol{\eta}}(i_1, i_2)$ of deformed image $I_2(\mathbf{x}-\mathbf{u})$ and image $I_1(\mathbf{x})$ as a continuous function using the Parzen windowing method.

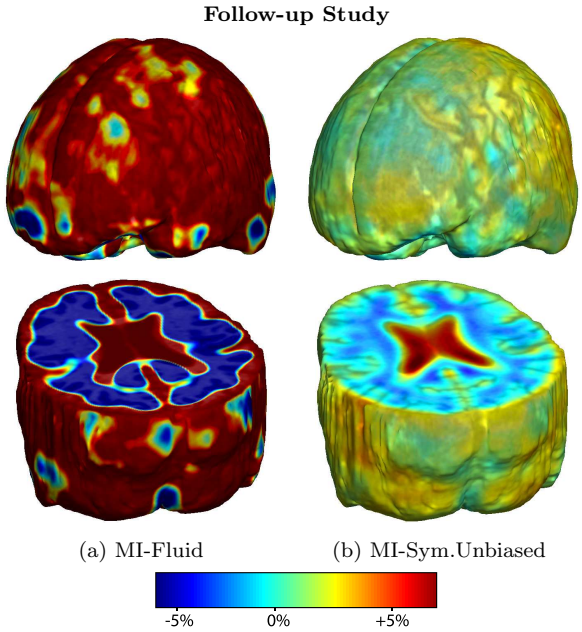

Fig. 16 Nonrigid registration was performed on the ADNI Follow-up study (serial MRI images of patients with Alzheimer's disease acquired 12 months apart) using MI-Fluid (column 1) and MI-Unbiased (column 2) registration methods. For each method, the mean of the resulting 10 Jacobian maps is superimposed on one of the brain volumes. Visually, MI-Fluid generates a noisy mean map, while the map generated using MI-Unbiased method suggests a volume reduction in gray matter as well as ventricular enlargement. The results obtained using the MI-Asymmetric Unbiased method are similar to those obtained using the MI-Unbiased method, and are therefore omitted.

We compute the first variation of $F_{MI}(\mathbf{u})$ by perturbing $\mathbf{u}$ in the following way

$$\frac{dF_{MI}(\mathbf{u}+\varepsilon\boldsymbol{\eta})}{d\varepsilon} = -\frac{d}{d\varepsilon}\int_{\mathbb{R}^2} p^{I_1,I_2}_{\mathbf{u}+\varepsilon\boldsymbol{\eta}}(i_1,i_2)\,\log\frac{p^{I_1,I_2}_{\mathbf{u}+\varepsilon\boldsymbol{\eta}}(i_1,i_2)}{p^{I_1}(i_1)p^{I_2}_{\mathbf{u}+\varepsilon\boldsymbol{\eta}}(i_2)}\,di_1di_2. \tag{49}$$

Thus, we have

$$\begin{aligned}\frac{dF_{MI}(\mathbf{u}+\varepsilon\boldsymbol{\eta})}{d\varepsilon} &= -\int_{\mathbb{R}^2}\left(1+\log\frac{p^{I_1,I_2}_{\mathbf{u}+\varepsilon\boldsymbol{\eta}}(i_1,i_2)}{p^{I_1}(i_1)p^{I_2}_{\mathbf{u}+\varepsilon\boldsymbol{\eta}}(i_2)}\right)\frac{dp^{I_1,I_2}_{\mathbf{u}+\varepsilon\boldsymbol{\eta}}(i_1,i_2)}{d\varepsilon}\,di_1di_2 \\ &\quad+\int_{\mathbb{R}^2}\frac{p^{I_1,I_2}_{\mathbf{u}+\varepsilon\boldsymbol{\eta}}(i_1,i_2)}{p^{I_2}_{\mathbf{u}+\varepsilon\boldsymbol{\eta}}(i_2)}\frac{dp^{I_2}_{\mathbf{u}+\varepsilon\boldsymbol{\eta}}(i_2)}{d\varepsilon}\,di_1di_2.\end{aligned} \tag{50}$$

However, note that

$$\int_{\mathbb{R}} p^{I_1,I_2}_{\mathbf{u}+\varepsilon\boldsymbol{\eta}}(i_1,i_2)\,di_1 = p^{I_2}_{\mathbf{u}+\varepsilon\boldsymbol{\eta}}(i_2) \tag{51}$$

and

$$\int_{\mathbb{R}} p^{I_2}_{\mathbf{u}+\varepsilon\boldsymbol{\eta}}(i_2)\,di_2 = 1. \tag{52}$$

Hence, the second term on the right hand side of the equality in (50) reduces to

$$\begin{aligned}&\int_{\mathbb{R}^2}\frac{p^{I_1,I_2}_{\mathbf{u}+\varepsilon\boldsymbol{\eta}}(i_1,i_2)}{p^{I_2}_{\mathbf{u}+\varepsilon\boldsymbol{\eta}}(i_2)}\frac{dp^{I_2}_{\mathbf{u}+\varepsilon\boldsymbol{\eta}}(i_2)}{d\varepsilon}\,di_1di_2 \\ &=\int_{\mathbb{R}}\frac{dp^{I_2}_{\mathbf{u}+\varepsilon\boldsymbol{\eta}}(i_2)}{d\varepsilon}\frac{1}{p^{I_2}_{\mathbf{u}+\varepsilon\boldsymbol{\eta}}(i_2)}\Big(\int_{\mathbb{R}} p^{I_1,I_2}_{\mathbf{u}+\varepsilon\boldsymbol{\eta}}(i_1,i_2)\,di_1\Big)\,di_2 \\ &=\int_{\mathbb{R}}\frac{dp^{I_2}_{\mathbf{u}+\varepsilon\boldsymbol{\eta}}(i_2)}{d\varepsilon}\frac{1}{p^{I_2}_{\mathbf{u}+\varepsilon\boldsymbol{\eta}}(i_2)}p^{I_2}_{\mathbf{u}+\varepsilon\boldsymbol{\eta}}(i_2)\,di_2 \\ &=\frac{d}{d\varepsilon}\int_{\mathbb{R}} p^{I_2}_{\mathbf{u}+\varepsilon\boldsymbol{\eta}}(i_2)\,di_2 = 0.\end{aligned} \tag{53}$$

Equation (49) becomes

$$\begin{aligned}\frac{dF_{MI}(\mathbf{u}+\varepsilon\boldsymbol{\eta})}{d\varepsilon} = -\int_{\mathbb{R}^2}\Bigg[&\left(1+\log\frac{p^{I_1,I_2}_{\mathbf{u}+\varepsilon\boldsymbol{\eta}}(i_1,i_2)}{p^{I_1}(i_1)p^{I_2}_{\mathbf{u}+\varepsilon\boldsymbol{\eta}}(i_2)}\right) \\ &\times\frac{dp^{I_1,I_2}_{\mathbf{u}+\varepsilon\boldsymbol{\eta}}(i_1,i_2)}{d\varepsilon}\Bigg]\,di_1di_2.\end{aligned} \tag{54}$$

The joint intensity distribution estimated from $I_2(\mathbf{x}-\mathbf{u})$ and $I_1(\mathbf{x})$ is given by

$$\begin{aligned}&p^{I_1,I_2}_{\mathbf{u}+\varepsilon\boldsymbol{\eta}}(i_1,i_2) = \\ &\frac{1}{|\Omega|}\int_{\Omega}\psi\Big(I_1(\mathbf{x})-i_1, I_2(\mathbf{x}-\mathbf{u}(\mathbf{x})-\varepsilon\boldsymbol{\eta}(\mathbf{x}))-i_2\Big)\,d\mathbf{x},\end{aligned} \tag{55}$$

where $|\Omega|$ is a volume of Ω and $\psi(\xi_1,\xi_2)$ is a two-dimensional Parzen windowing kernel.

The derivative of (55) can also be computed:

$$\begin{aligned}&\frac{dp^{I_1,I_2}_{\mathbf{u}+\varepsilon\boldsymbol{\eta}}(i_1,i_2)}{d\varepsilon} \\ &=-\frac{1}{|\Omega|}\int_{\Omega}\frac{\partial\psi}{\partial\xi_2}\Big(I_1(\mathbf{x})-i_1, I_2(\mathbf{x}-\mathbf{u}(\mathbf{x})-\varepsilon\boldsymbol{\eta}(\mathbf{x}))-i_2\Big) \\ &\qquad\times\nabla I_2(\mathbf{x}-\mathbf{u}(\mathbf{x})-\varepsilon\boldsymbol{\eta}(\mathbf{x}))\cdot\boldsymbol{\eta}(\mathbf{x})\,d\mathbf{x}.\end{aligned} \tag{56}$$

Let us denote

$$Q_{\mathbf{u}}(i_1,i_2) = 1+\log\frac{p^{I_1,I_2}_{\mathbf{u}}(i_1,i_2)}{p^{I_1}(i_1)p^{I_2}_{\mathbf{u}}(i_2)}. \tag{57}$$

If we let $\varepsilon=0$, equation (54) gives the first variation of $F_{MI}(\mathbf{u})$:

$$\begin{aligned}&\frac{dF_{MI}(\mathbf{u}+\varepsilon\boldsymbol{\eta})}{d\varepsilon}\Big|_{\varepsilon=0} \\ &=\int_{\mathbb{R}^2}Q_{\mathbf{u}}(i_1,i_2)\frac{1}{|\Omega|}\int_{\Omega}\frac{\partial\psi}{\partial\xi_2}(I_1(\mathbf{x})-i_1, I_2(\mathbf{x}-\mathbf{u}(\mathbf{x}))-i_2) \\ &\qquad\times\nabla I_2(\mathbf{x}-\mathbf{u}(\mathbf{x}))\cdot\boldsymbol{\eta}(\mathbf{x})\,d\mathbf{x}\,di_1di_2 \\ &=\frac{1}{|\Omega|}\int_{\Omega}\left[Q_{\mathbf{u}}*\frac{\partial\psi}{\partial\xi_2}\right](I_1(\mathbf{x}), I_2(\mathbf{x}-\mathbf{u}(\mathbf{x})))\\ &\times\nabla I_2(\mathbf{x}-\mathbf{u}(\mathbf{x}))\cdot\boldsymbol{\eta}(\mathbf{x})\,d\mathbf{x}.\end{aligned} \tag{58}$$

Here, $*$ denotes a convolution. Thus,

$$\partial_{\mathbf{u}}F_{MI}(\mathbf{u}) = \frac{1}{|\Omega|}\left[Q_{\mathbf{u}}*\frac{\partial\psi}{\partial\xi_2}\right](I_1(\mathbf{x}), I_2(\mathbf{x}-\mathbf{u}))\nabla I_2(\mathbf{x}-\mathbf{u}). \tag{59}$$

References

1. P. M. Thompson and A. W. Toga, "A framework for computational anatomy," *Computing and Visualization in Science*, vol. 5, pp. 13–34, 2002.

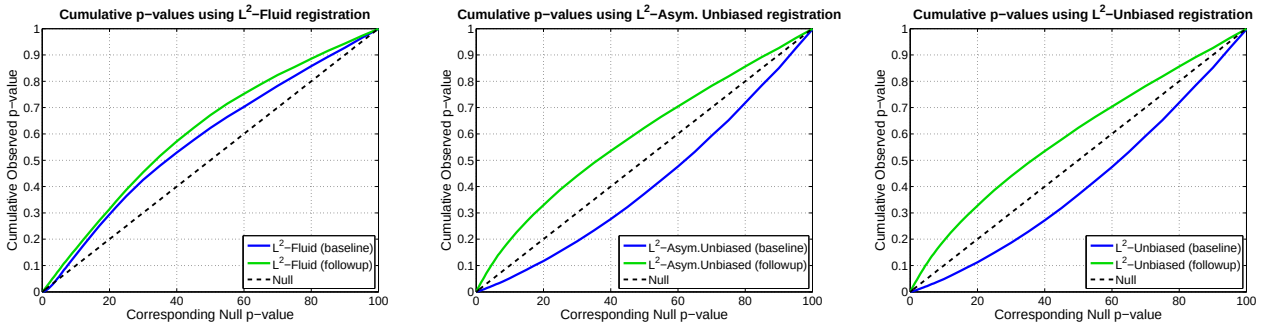

(a) (b) (c)

Fig. 17 Cumulative distribution of p-values for the voxelwise log Jacobian t-maps (as defined in Equation (36)) for both ADNI Baseline (in blue) and Follow-up (in green) using (a) L^2-Fluid, (b) L^2-Asymmetric Unbiased, and (c) L^2-Symmetric Unbiased methods. Here, a better method should separate these two CDF plots (see Section 5.4) with the Null line in between, indicating a real biological change has occurred between these two time points. Hence, L^2-Asymmetric Unbiased and L^2-Symmetric Unbiased methods outperform L^2-Fluid method. Note that the interval $p \in [0, 0.05]$ is of most importance for observation.

2. U. Grenander and M. I. Miller, "Computational anatomy: An emerging discipline," *Quarterly of Applied Mathematics*, vol. 56, pp. 617–694, 1998.
3. M. K. Chung, K. J. Worsley, T. Paus, C. Cherif, D. L. Collins, J. N. Giedd, J. L. Rapoport, and A. C. Evans, "A unified statistical approach to deformation-based morphometry," *NeuroImage*, vol. 14, pp. 595–606, 2001.
4. B. Avants and J. C. Gee, "Geodesic estimation for large deformation anatomical shape averaging and interpolation," *NeuroImage*, vol. 23, suppl. 1, pp. S139–50, 2004.
5. D. Shen and C. Davatzikos, "Very high-resolution morphometry using mass-preserving deformations and HAMMER elastic registration," *NeuroImage*, vol. 18, no. 1, pp. 28–41, 2003.
6. G. Christensen, R. Rabbitt, and M. Miller, "Deformable templates using large deformation kinematics," *IEEE Transactions on Image Processing*, vol. 5, no. 10, pp. 1435–1447, 1996.
7. M. I. Miller, "Computational anatomy: shape, growth, and atrophy comparison via diffeomorphisms," *NeuroImage*, vol. 23, suppl. 1, pp. S19–S33, 2004.
8. D. L. Collins, T. M. Peters, and A. C. Evans, "Automated 3D nonlinear deformation procedure for determination of gross morphometric variability in human brain," in *Proceedings of the International Society for Optical Engineering (SPIE) 2359*, 1994, pp. 180–190.
9. A. Leow, S.-C. Huang, A. Geng, J. Becker, S. Davis, A. Toga, and P. Thompson, "Inverse consistent mapping in 3D deformable image registration: Its construction and statistical properties," *Information Processing in Medical Imaging*, vol. 3752, pp. 493–503, 2005.
10. L. Wang, J. Swank, I. Glick, M. Gado, M. Miller, J. Morris, and J. Csernansky, "Changes in hippocampal volume and shape across time distinguish dementia of the Alzheimer type from healthy aging," *NeuroImage*, vol. 20, pp. 667–682, 2003.
11. B. Ridha, J. Barnes, J. Bartlett, A. Godbolt, T. Pepple, M. Rossor, and N. Fox, "Tracking atrophy progression in familial Alzheimer's disease: a serial MRI study," *The Lancet Neurology*, vol. 5, pp. 828–834, 2006.
12. W. Crum, R. Scahill, and N. Fox, "Automated hippocampal segmentation by regional fluid registration of serial MRI: validation and application in Alzheimer's disease," *NeuroImage*, vol. 13, pp. 847–855, 2001.
13. R. Hogan, L. Mark, L. Wang, S. Joshi, M. Miller, and R. Bucholz, "Mesial temporal sclerosis and temporal lobe epilepsy: MR imaging deformation-based segmentation of the hippocampus in five patients," *Radiology*, vol. 216, pp. 291–297, 2000.
14. A. Leow, I. Yanovsky, M.-C. Chiang, A. Lee, A. Klunder, A. Lu, J. Becker, S. Davis, A. Toga, and P. Thompson, "Statistical properties of Jacobian maps and the realization of unbiased large-deformation nonlinear image registration," *IEEE Transactions on Medical Imaging*, vol. 26, no. 6, pp. 822–832, 2007.
15. I. Yanovsky, P. Thompson, S. Osher, and A. Leow, "Topology preserving log-unbiased nonlinear image registration: Theory and implementation," *IEEE Conference on Computer Vision and Pattern Recognition*, pp. 1–8, June 2007.
16. A. Leow, A. Klunder, C. Jack, A. Toga, A. Dale, M. Bernstein, P. Britson, J. Gunter, C. Ward, J. Whitwell, B. Borowski, A. Fleisher, N. Fox, D. Harvey, J. Kornak, N. Schuff, C. Studholme, G. Alexander, M. Weiner, and P. Thompson, "Longitudinal stability of MRI for mapping brain change using tensor-based morphometry," *NeuroImage*, vol. 31, no. 2, pp. 627–40, 2006.
17. C. Jack, M. Bernstein, N. Fox, P. Thompson, G. Alexander, D. Harvey, B. Borowski, P. Britson, J. Whitwell, C. Ward, A. Dale, J. Felmlee, J. Gunter, D. Hill, R. Killiany, N. Schuff, S. Fox-Bosetti, C. Lin, C. Studholme, C. DeCarli, G. Krueger, H. Ward, G. Metzger, K. Scott, R. Mallozzi, D. Blezek, J. Levy, J. Debbins, A. Fleisher, M. Albert, R. Green, G. Bartzokis, G. Glover, J. Mugler, and M. Weiner, "The Alzheimer's Disease Neuroimaging Initiative (ADNI): The MR imaging protocol," *Journal of MRI*, 2007, in press.
18. J. Jovicich, S. Czanner, D. Greve, E. Haley, A. van der Kouwe, R. Gollub, D. Kennedy, F. Schmitt, G. Brown, J. MacFall, B. Fischl, and A. Dale, "Reliability in multi-site structural MRI studies: Effects of gradient non-linearity correction on phantom and human data," *NeuroImage*, vol. 30, no. 2, pp. 436–443, 2006.
19. J. Sled, A. Zijdenbos, and A. Evans, "A nonparametric method for automatic correction of intensity nonuniformity in MRI data," *IEEE Transactions on Medical Imaging*, vol. 17, pp. 87–97, 1998.
20. J. Gunter, M. Bernstein, B. Borowski, J. Felmlee, D. Blezek, and R. Mallozzi, "Validation testing of the MRI calibration phantom for the Alzheimer's Disease Neuroimaging Initiative study," *ISMRM 14th Scientific Meeting and Exhibition*, 2006.

21. P. Viola and W. M. Wells, "Alignment by maximization of mutual information," *International Conference on Computer Vision*, pp. 16–23, 1995.
22. A. Collignon, F. Maes, D. Delaere, D. Vandermeulen, P. Suetens, and G. Marchal, "Automated multi-modality image registration based on information theory," in *Information Processing in Medical Imaging*, Y. Bizais, C. Barillot, and R. Di Paola, Eds., vol. 3. Kluwer Academic Publishers, Dordrecht, 1995, pp. 264–274.
23. G. Hermosillo, C. Chefd'Hotel, and O. Faugeras, "A variational approach to multi-modal image matching," *INRIA Research report 4117*, 2001.
24. W. M. Wells, P. Viola, H. Atsumi, S. Nakajima, and R. Kikinis, "Multi-modal volume registration by maximization of mutual information," *Medical Image Analysis*, vol. 1, no. 1, pp. 35–51, 1996.
25. E. D'Agostino, F. Maes, D. Vandermeulen, and P. Suetens, "A viscous fluid model for multimodal non-rigid image registration using mutual information," *Medical Image Analysis*, vol. 7, pp. 565–575, 2003.
26. J. C. Mazziotta, A. W. Toga, A. C. Evans, P. T. Fox, J. Lancaster, K. Zilles, R. P. Woods, T. Paus, G. Simpson, B. Pike, C. J. Holmes, D. L. Collins, P. M. Thompson, D. MacDonald, T. Schormann, K. Amunts, N. Palomero-Gallagher, L. Parsons, K. L. Narr, N. Kabani, G. Le Goualher, D. Boomsma, T. Cannon, R. Kawashima, and B. Mazoyer, "A probabilistic atlas and reference system for the human brain," *Journal of the Royal Society*, vol. 356, no. 1412, pp. 1293–1322, 2001.
27. E. Bullmore, J. Suckling, S. Overmeyer, S. Rabe-Hesketh, E. Taylor, and M. Brammer, "Global, voxel, and cluster tests, by theory and permutation, for a difference between two groups of structural MR images of the brain," *IEEE Transactions on Medical Imaging*, vol. 18, pp. 32–42, 1999.
28. T. Nichols and A. Holmes, "Nonparametric analysis of PET functional neuroimaging experiments: A primer," *Human Brain Mapping*, vol. 15, pp. 1–25, 2001.
29. K. Friston, A. Holmes, K. Worsley, J. Poline, C. Frith, and R. Frackowiak, "Statistical parametric maps in functional imaging: A general linear approach," *Human Brain Mapping*, vol. 2, pp. 189–210, 1995.
30. M. Chiang, R. Dutton, K. Hayashi, O. Lopez, H. Aizenstein, A. Toga, J. Becker, and P. Thompson, "3D pattern of brain atrophy in HIV/AIDS visualized using tensor-based morphometry," *NeuroImage*, vol. 34, pp. 44–60, 2007.
31. C. Brun, N. Lepore, X. Pennec, Y. Chou, O. Lopez, H. Aizenstein, J. Becker, A. Toga, and P. Thompson, "Comparison of standard and Riemannian elasticity for tensor-based morphometry in HIV/AIDS," in *MICCAI, Brisbane, Australia*, 2007.
32. N. Lepore, C. Brun, X. Pennec, Y. Chou, O. Lopez, H. Aizenstein, J. Becker, A. Toga, and P. Thompson, "Mean template for tensor-based morphometry using deformation tensors," in *MICCAI, Brisbane, Australia*, 2007.
33. J. H. Morra, Z. Tu, L. G. Apostolova, A. Green, A. W. Toga, and P. M. Thompson, "Comparison of Adaboost and support vector machines for detecting Alzheimer's disease through automated hippocampal segmentation," 2007, submitted for publication.
34. Y. Benjamini and Y. Hochberg, "Controlling the false discovery rate: a practical and powerful approach to multiple testing," *Journal of the Royal Statistical Society*, vol. B 57, pp. 289–300, 1995.
35. C. Genovese, N. Lazar, and T. Nichols, "Thresholding of statistical maps in functional neuroimaging using the false discovery rate," *Neuroimage*, vol. 15, pp. 870–878, 2002.
36. J. Storey, "A direct approach to false discovery rates," *Journal of the Royal Statistical Society*, vol. B 64, pp. 479–498, 2002.
37. H. Zhu, J. Ibrahim, N. Tang, D. Rowe, H. Xuejun, R. Bansal, and B. Petersen, "A statistical analysis of brain morphology using wild bootstrapping," *IEEE Transactions on Medical Imaging*, vol. 26, pp. 954–966, 2007.
38. G. E. Christensen and H. J. Johnson, "Consistent image registration," *IEEE Transactions on Medical Imaging*, vol. 20, no. 7, pp. 568–582, 2001.
39. C. Chefd'Hotel, G. Hermosillo, and O. Faugeras, "A variational approach to multi-modal image matching," *IEEE Workshop in Variational and Level Set Methods*, pp. 21–28, 2001.